1997-01-15

Wind-forced modeling studies of currents, meanders, and eddies in the California Current system

Batteen, Mary L.

Journal of Geophysical Research, Vol. 102, No. C1, pp. 985-1010, January 15, 1997.
http://hdl.handle.net/10945/47166

JOURNAL OF GEOPHYSICAL RESEARCH, VOL. 102, NO. C1, PAGES 985–1010, JANUARY 15, 1997

Wind-forced modeling studies of currents, meanders, and eddies in the California Current system

Mary L. Batteen

Department of Oceanography, Naval Postgraduate School, Monterey, California

Abstract. This process-oriented study of the California Current system (CCS) uses a high-resolution, multilevel, primitive equation ocean model on a β plane to isolate the response of that eastern boundary oceanic regime to temporal and spatially varying wind forcing. To study the generation, evolution, and maintenance of many of the observed features such as currents, meanders, and eddies in the CCS, the model is forced from rest with seasonal climatological winds. In response to the prevailing wind direction, surface equatorward currents develop, along with upwelling of cooler water along the coast and a poleward undercurrent. Baroclinic/barotropic instabilities in the equatorward surface current and poleward undercurrent result in the generation of meanders near the coast. As the meanders intensify, cold upwelling filaments develop along the coast and subsequently extend farther offshore. In time, the meanders form both cyclonic and anticyclonic eddies, which subsequently propagate farther offshore. Longer simulation times (~3–4 years), in which a quasi-equilibrium state for the CCS is reached, show a seasonal cycle in response to the wind forcing for the coastal currents, upwelling, and filaments. The meanders and eddies, however, can be quasi-permanent as well as seasonal features. The quasi-permanent features play a significant role in modifying coastal currents, upwelling, and filaments, which leads to large temporal and spatial variability in the CCS. In a sensitivity study, the results from several numerical experiments are used to examine the dependence of the generation of the currents, meanders, and eddies on the type of Coriolis parameterization, wind forcing, and coastline geometry. Both the meridional variability of f (β plane) and the alongshore component of the wind stress are shown to be key ingredients for generating realistic vertical and horizontal structures for the cores of the surface equatorward and the subsurface poleward currents. With such structures the currents are baroclinically and barotropically unstable, resulting in the generation of meanders, filaments, and eddies. Irregularities in the coastline geometry are shown to be important for "anchoring" upwelling and filaments as well as for enhancing the growth of meanders and eddies. Cyclonic eddies tend to form in the vicinity of capes, while anticyclonic eddies tend to form in the coastal indentations between capes. The region off Cape Blanco is identified as the location where the coastal, equatorward flow off Oregon leaves the coast to develop a meandering jet off California. The results from these experiments support the hypothesis that wind forcing and coastline irregularities on a beta plane are important mechanisms for the generation of many of the observed features of the CCS.

1. Introduction

1.1. Observational and Modeling Background

The climatological mean California Current system (CCS) is a classical eastern boundary current (EBC) system, which consists of several large-scale currents (see Figure 1). The predominant flow is the California Current (CC), which, in the mean, is a broad (~1000 km), relatively slow (~10–30 cm/s), equatorward surface flow. It flows year-round, and extends to ~500 m depth. The second basic flow is the California Undercurrent (CUC), which is a narrower (~10–40 km), relatively weak (~2–10 cm/s), poleward subsurface flow. It can vary seasonally and is strongest at ~300 m depth. The third flow component is the Inshore Current (IC), which is known as the Davidson Current (DC) north of Point Conception. This is also a relatively weak (~5 cm/s) poleward flow, which is found at the surface and near the coast. There are other ICs known as the Southern California Countercurrent (SCC) to the south, and the Southern California Eddy (SCE) inshore of the Channel Islands within the California Bight [*Hickey*, 1979, 1996].

Recent studies have shown that the CCS is not the quiescent, stable system of currents with a well-defined, unchanging structure suggested by Figure 1. Rather, the flow fluctuates greatly in both time and space [*Chelton*, 1984]. Irregularities in the flow were noted as early as 1950 [*Reid*, 1988]. There exist mesoscale meanders, eddies, filaments and jet-like surface currents, which are superimposed on the large-scale flow [*Bernstein et al.*, 1977; *Chelton*, 1984; *Mooers and Robinson*, 1984; *Robinson et al.*, 1984; *Rienecker et al.*, 1985, 1988; *Rienecker and Mooers*, 1989; *Brink and Cowles*, 1991; *Strub et al.*, 1991]. Eddy-like features with wavelengths of the order of 100 km [*Freitag and Halpern*, 1981; *Bernstein et al.*, 1977] have been documented and are prevalent in most satellite observations [e.g.,

Paper number 96JC02803.

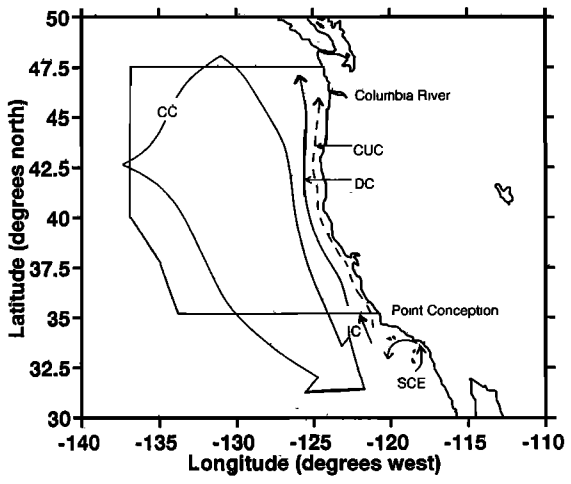

Figure 1. Generalized circulation schematic of the classical climatological California Current system (CCS). The broad, slow surface equatorward California Current (CC) overlies the poleward California Undercurrent (CUC) along with the Inshore Current (IC), known as the Davidson Current (DC) north of Point Conception and as the Southern California Eddy (SCE) south of Point Conception. The box shows the domain of the model for the basic study (experiment 1) off the western coast of the United States of America. The domain is bounded by 35° to 47.5°N and from the coast to 12.5° offshore and covers an area 1024 km (1408 km) in the cross-shore (alongshore) direction. The cross-shore (alongshore) resolution is 8 km (11 km).

Ikeda and Emery, 1984; *Ikeda et al.*, 1984a, b; *Kelly*, 1985]. The current itself may take the form of a meandering jet, with wavelengths of ~100 to 300 km [*Bernstein et al.*, 1977]. Cold, offshore flowing filaments, which can exhibit a 1°–3°C temperature change across their boundaries [*Bernstein et al.*, 1977], are associated with these meanders. The filaments can extend to ~100–200 m depth, with a width of ~20–100 km at the surface, and with peak speeds of ~50–100 cm/s [*Mooers and Robinson*, 1984; *Rienecker et al.*, 1985; *Rienecker and Mooers*, 1989; *Flament et al.*, 1985; *Kosro and Huyer*, 1986; *Brink and Cowles*, 1991]. The combination of these features has led to a new conceptualization of the CCS as a system of currents with filamented jets and mesoscale eddies modifying the mean flow [*Mooers and Robinson*, 1984].

The dynamical processes responsible for the generation and evolution of these intense and complex meander, eddy, and filament structures in the CCS have yet to be fully identified [*Strub et al.*, 1991]. A possible generative mechanism arises from the baroclinic and/or barotropic instability of the mean coastal CCS, which, during the upwelling season (approximately April through September) consists of the equatorward CC overlying the poleward CUC. This generative mechanism was explored first in modeling studies by *Ikeda and Emery* [1984] and *Ikeda et al.* [1984a, b], and most recently by *Haidvogel et al.* [1991]. In these studies, externally prescribed, longshore currents (representing the coastal jet and/or undercurrent) have been imposed and subsequently studied by analyzing the conditions that cause these currents to become unstable. The linear stability analysis of *Ikeda et al.* [1984a] has suggested that baroclinic instability can be an important process for generating meanders. Studies by *Ikeda et al.* [1984a, b], which incorporated the additional features of bumps to represent capes and ridges, have shown that the bumps can help trigger baroclinic instability, but the basic instability still results from the opposing alongshore currents. *Haidvogel et al.* [1991] prescribed an equatorward coastal jet in a model with bottom topography and irregular coastline geometry incorporated. Their results showed that the growth of instabilities was enhanced by coastline and/or topographic irregularities. An examination of these and other stability analyses [e.g., *Pierce et al.*, 1991; *Allen et al.*, 1991], laboratory modeling [e.g., *Narimousa and Maxworthy*, 1985, 1989], and numerical modeling [e.g., *Walstad et al.*, 1991] of filament dynamics have led to the conclusion that finite amplitude instabilities of the CC can account for the origin and much of the behavior of observed filaments in the CCS [*Brink and Cowles*, 1991].

Another generative mechanism for the observed features in the CCS is wind forcing, which may be the most important mechanism for the generation of the currents as well as for the intense and complex meander, eddy, jet, and filament structures in the CCS. The wind forcing can set up the coastal currents, which can subsequently become unstable and lead to the formation of many of the features observed in the CCS. (In the modeling studies discussed above, the CC was prescribed rather than generated.) Satellite infrared imagery has shown evidence of these features during periods of winds favorable for upwelling, which suggests that wind forcing is a possible important mechanism for the formation of these features.

This generative mechanism in the CCS has been explored by *Batteen et al.* [1989], *McCreary et al.* [1991], *Auad et al.* [1991], and *Pares-Sierra et al.* [1993]. In these model studies, externally imposed currents are not necessary; rather, the wind-forced models develop their own currents, which can subsequently become unstable. Here we briefly highlight some of the results from these studies, since they are relevant to the present study.

In the 10-level, primitive equation (PE) modeling study of *Batteen et al.* [1989], the response to wind forcing in the central CCS region was examined using a band of steady, equatorward (upwelling favorable) winds. After about 30–40 days a wind-driven equatorward coastal jet and poleward undercurrent developed. Owing to both barotropic and baroclinic instability processes, the coastal jet and undercurrent became unstable and led to the development of a meandering coastal jet and several relatively weak eddies of 50 km or less in diameter. Note that although this was the first wind-forced model to generate a meandering jet and eddies in the CCS, no large-scale eddies or elongated filaments were generated, presumably on account of the relatively short simulation time of 90 days for each experiment.

McCreary et al. [1991] used a 2½-layer PE model with a band of steady, equatorward winds. Since the model was a layer rather than a level model, it included entrainment of cool water into the upper layer. The entrainment cooled the sea surface temperature, provided interfacial stress, and prevented the interface from surfacing in upwelling regions. The background of a sharp coastal front was also incorporated into the model to allow frontal instabilities to be studied. The results showed that a surface jet, an undercurrent, and an upwelling front could be generated. Due to frontal instabilities (which *McCreary et al.* [1991] said required an upper layer temperature gradient), small-scale, fingerlike disturbances were generated, which subsequently grew in amplitude and scale. Eventually, upwelling filaments and eddies were also generated by the model.

Pares-Sierra et al. [1993] used both an 8-layer, quasi-

geostrophic (QG) model and a 1½-layer PE model to study the generation of coastal, mesoscale eddy activity in the CCS. While the QG model could represent baroclinic instability but not the coastal response to winds, the PE model could represent the coastal response to winds but not baroclinic instability (being a 1½-layer model). With these limitations, the results showed, as expected, that baroclinic instability dominated the response of the QG CCS model, while local wind forcing at the coast dominated the response of the PE CCS model. Similar results with the QG model were obtained by *Auad et al.* [1991].

1.2. Present Research

This process-oriented study builds on the previous studies by using a multilevel PE model to isolate the effects of temporally and spatially varying wind forcing on the generation, evolution, and maintenance of currents, meanders, and eddies in the CCS. In a sensitivity study, results from several numerical experiments will be examined to understand the dependence of the generation of the currents, meanders, and eddies on the type of wind forcing, Coriolis parameterization, and coastline geometry used.

The use of a 10-level model rather than a 1½-layer model (as used by *Pares-Sierra et al.* [1993]) allows baroclinic instability processes to be studied, while the use of a PE rather than a QG model (as used by *Auad et al.* [1991]) allows the coastal response to winds to be represented. To isolate the effects of baroclinic/barotropic instability from possible coupled effects of wind forcing with frontal instability processes (which *McCreary et al.* [1991] investigated), the model will be initialized with a horizontally uniform climatological temperature profile. Note that since the model is level, entrainment of cool water into the upper layer(s) is not necessary. To allow larger-scale eddies and elongated filaments to be generated, simulation times longer (i.e., ~3–4 years) than 90 days (which *Batteen et al.* [1989] was limited to) will be used.

This study is organized as follows: The PE model and the experimental conditions used in the basic study are presented in section 2. The results of the basic model simulations are described in section 3, while section 4 explores the dependence of the generation of currents, meanders, and eddies on the type of Coriolis parameterization, wind forcing, and coastline geometry used. A summary and a discussion are presented in section 5.

2. Model Description

2.1. Model Equations

The numerical model in this study was originally used for a coarse-resolution, closed basin by *Haney* [1974] and later adapted for eddy-resolving, limited-area EBC regions with open borders on the northern, western, and southern boundaries by *Batteen* [1989], *Batteen and Rutherford* [1990], and *Batteen et al.* [1989, 1992a, b, 1995]. The limited-area EBC model is multilevel, uses nonadiabatic primitive equations on a β-plane, and has both baroclinic and barotropic velocity components. The model is based on the hydrostatic and Boussinesq approximations. The governing equations are as follows:

$$\frac{du}{dt} = \frac{-1}{\rho_0}\frac{\partial p}{\partial x} + fv - A_M\nabla^4 u + K_M\frac{\partial^2 u}{\partial z^2} + \delta_d(u) \quad (1)$$

$$\frac{dv}{dt} = \frac{-1}{\rho_0}\frac{\partial p}{\partial y} - fu - A_M\nabla^4 v + K_M\frac{\partial^2 v}{\partial z^2} + \delta_d(v) \quad (2)$$

Table 1. Values of Constants Used in the Model

Constant	Value	Definition
T_0	278.2°K	constant reference temperature
ρ_a	1.23×10^{-3} g cm^{-3}	density of air
ρ_0	1.0276 g cm^{-3}	density of seawater at T_0
α	2.4×10^{-4} (°K)$^{-1}$	thermal expansion coefficient
C	0.958 cal g^{-1} (°K)$^{-1}$	specific heat of seawater
C_D	1.225×10^{-3}	bottom drag coefficient
K	10	number of levels in vertical
Δx	8×10^5 cm	cross-shore grid spacing
Δy	1.1×10^6 cm	alongshore grid spacing
H	4.5×10^5 cm	total ocean depth
Δt	800 s	time step
f_0	0.96×10^4 s^{-1}	mean Coriolis parameter
g	980 cm s^{-2}	acceleration of gravity
A_M	2×10^{17} cm^4 s^{-1}	biharmonic momentum diffusion coefficient
A_H	2×10^{17} cm^4 s^{-1}	biharmonic heat diffusion coefficient
K_M	0.5 cm^2 s^{-1}	vertical eddy viscosity
K_H	0.5 cm^2 s^{-1}	vertical eddy conductivity

$$\frac{\partial u}{\partial x} + \frac{\partial v}{\partial y} + \frac{\partial w}{\partial z} = 0 \quad (3)$$

$$\frac{\partial p}{\partial z} = -\rho g \quad (4)$$

$$\rho = \rho_0[1 - \alpha(T - T_0)] \quad (5)$$

$$\frac{dT}{dt} = -A_H\nabla^4 T + K_H\frac{\partial^2 T}{\partial z^2} + \delta_d(T) \quad (6)$$

In the above equations; t is time, (x, y, z) is a right-handed Cartesian coordinate system with x pointing toward shore, y alongshore, and z upward; (u, v, w) are the corresponding velocity components; T is temperature; ρ is density; and p is pressure. Table 1 provides a list of other symbols found in the model equations, as well as values of constants used throughout the study.

The terms $\delta_d(u)$, $\delta_d(v)$ and $\delta_d(T)$ in equations (1), (2), and (6), respectively, represent the vertical turbulent mixing of momentum and heat due to surface layer processes, by a dynamic adjustment mechanism. This adjustment, a generalization of the convective adjustment mechanism, is based on the assumption of a critical Richardson number, and it serves to maintain dynamic stability in the water column [*Adamec et al.*, 1981; *Adamec*, 1986].

The boundary conditions at the top ($z = 0$) of the model ocean are

$$K_M\frac{\partial u}{\partial z} = \frac{\tau^x}{\rho_0} \quad (7)$$

$$K_M\frac{\partial v}{\partial z} = \frac{\tau^y}{\rho_0} \quad (8)$$

$$K_H\frac{\partial T}{\partial z} = Q_S - Q_B \quad (9)$$

$$w = 0 \quad (10)$$

In (7) and (8), τ^x and τ^y are the cross-shore and alongshore components, respectively, of the surface wind stress. In (9), Q_B is the net upward flux of longwave radiation and sensible and

latent heat flux across the sea surface, and $Q_S = (1/\rho_0 C)(\partial S/\partial z)$ is the heating due to solar radiation, with

$$S = S_0(Re^{z/z_1} + (1 - R)e^{z/z_2}) \tag{11}$$

Here S_0 is the downward flux of solar radiation at the surface, $R = 0.62$ is the fraction of solar radiation absorbed in the upper few meters ($z_1 = 1.5$ m), and $(1 - R) = 0.38$ is the fraction that penetrates to somewhat deeper levels ($z_2 = 20$ m), as given by *Paulson and Simpson* [1977]. Equation (10) is the rigid lid approximation, which filters out external gravity waves and allows a longer time step, determined by the phase speed of internal waves, to be used.

The bottom ($z = -H$) boundary conditions are as follows:

$$K_M \frac{\partial u}{\partial z} = C_D(u^2 + v^2)^{1/2}(u \cos \gamma - v \sin \gamma) \tag{12}$$

$$K_M \frac{\partial v}{\partial z} = C_D(u^2 + v^2)^{1/2}(v \cos \gamma + u \sin \gamma) \tag{13}$$

$$K_H \frac{\partial T}{\partial z} = 0 \tag{14}$$

$$w = -u \frac{\partial H}{\partial x} - v \frac{\partial H}{\partial y} \tag{15}$$

In (12) and (13), C_D is a bottom drag coefficient and $\gamma = 10°$ is the geostrophic inflow angle [*Weatherly*, 1972]. The bottom stress in (12) and (13) represents one of the simplest parameterizations of a bottom Ekman layer. The boundary conditions on the ocean bottom in (14) and (15) are those of no vertical heat flux and flow required to parallel the slope.

2.2. Method of Solution

Equations (1)–(6) constitute a closed system of six scalar equations and six unknowns, u, v, w, p, ρ, and T. The variables u, v, and T are prognostic variables whose time rates of change are predicted from (1), (2), and (6), respectively. Although the diagnostic variables w, p, and ρ can be determined from (3), (4), and (5), respectively, there are additional constraints imposed on p and w by the choice of the rigid lid boundary conditions. The vertically integrated pressure can no longer be obtained by integrating the hydrostatic equation (4) for the free surface. Further, the vertically integrated horizontal velocity is constrained to be nondivergent, i.e.,

$$\int_{-H}^{0} \left(\frac{\partial u}{\partial x} + \frac{\partial v}{\partial y}\right) d\varepsilon = 0 \tag{16}$$

which is obtained by integrating (3) and applying the vertical boundary conditions.

For any quantity $\mathbf{q}$, let its vertical average be denoted by $\bar{q}$ and its departure (vertical shear) be denoted by q'. From (16) the vertical mean flow can then be described by a stream function ψ, such that

$$\bar{u} = -\frac{1}{H}\frac{\partial \psi}{\partial y} \tag{17}$$

$$\bar{v} = \frac{1}{H}\frac{\partial \psi}{\partial x} \tag{18}$$

The stream function ψ is predicted from the vorticity equation, which is derived from the vertical average of (1) and (2). Applying the curl operator to the vertical average of (1) and (2), and using (17) and (18), the vorticity equation is

$$\begin{aligned}\frac{\partial \zeta}{\partial t} = {} & \frac{\partial}{\partial t}\left[\frac{1}{H}\left(\frac{\partial^2 \psi}{\partial x^2}\right) + \frac{1}{H}\left(\frac{\partial^2 \psi}{\partial y^2}\right) + \frac{\partial \psi}{\partial x}\frac{\partial H^{-1}}{\partial x} + \frac{\partial \psi}{\partial y}\frac{\partial H^{-1}}{\partial y}\right] \\ = {} & -\left[\frac{\partial}{\partial x}\left(\frac{f}{H}\frac{\partial \psi}{\partial y}\right) - \frac{\partial}{\partial y}\left(\frac{f}{H}\frac{\partial \psi}{\partial x}\right)\right] \\ & -\left[\frac{\partial}{\partial x}\left(\frac{g}{H\rho_0}\int_{-H}^{0}\int_{z}^{0}\frac{\partial \rho}{\partial y}\,d\varepsilon\,dz\right)\right. \\ & \left. -\frac{\partial}{\partial y}\left(\frac{g}{H\rho_0}\int_{-H}^{0}\int_{z}^{0}\frac{\partial \rho}{\partial x}\,d\varepsilon\,dz\right)\right] \\ & +\frac{\partial}{\partial x}\left(\frac{1}{H}\int_{-H}^{0} G\,dz\right) - \frac{\partial}{\partial y}\left(\frac{1}{H}\int_{-H}^{0} F\,dz\right)\end{aligned} \tag{19}$$

where G and F represent the collected contributions of the nonlinear and viscous terms in (1) and (2).

The vorticity equation (19) is solved by obtaining an updated value of ζ by application of the leapfrog (or, every 11 time steps, the Euler-backward) time-differencing scheme. The associated value of ψ can then be obtained from

$$\zeta = \frac{1}{H}\left(\frac{\partial^2 \psi}{\partial x^2}\right) + \frac{1}{H}\left(\frac{\partial^2 \psi}{\partial y^2}\right) + \frac{\partial \psi}{\partial x}\frac{\partial H^{-1}}{\partial x} + \frac{\partial \psi}{\partial y}\frac{\partial H^{-1}}{\partial y} \tag{20}$$

which is an elliptic equation. A solution to (20) is fully prescribed by specifying the values of ψ on the open and closed boundaries of the model domain. Currently, to solve (20), the model uses an elliptic solver when there are no variations in coastline geometry, and/or topography, and successive overrelaxation techniques when there are variations in coastline geometry and/or topography.

The vertical shear current (u', v') is predicted from (1) and (2) after subtracting the vertical mean. The results are

$$\frac{\partial u'}{\partial t} = \frac{-1}{\rho_0}\frac{\partial p'}{\partial x} + fv' - A_M\nabla^4 u' + K_M\frac{\partial^2 u'}{\partial z^2} + F - \bar{F} - \frac{\tau^y}{\rho_0 H} \tag{21}$$

$$\frac{\partial v'}{\partial t} = \frac{-1}{\rho_0}\frac{\partial p'}{\partial y} - fu' - A_M\nabla^4 v' + K_M\frac{\partial^2 v'}{\partial z^2} + G - \bar{G} - \frac{\tau^x}{\rho_0 H} \tag{22}$$

In (21) and (22), p', which represents the departure of the pressure from the vertical average, is, using (4), expressed in terms of ρ as

$$p' = \int_{z}^{0} \rho g\,d\varepsilon - \frac{1}{H}\int_{-H}^{0}\left(\int_{z}^{0}\rho g\,d\varepsilon\right)dz \tag{23}$$

where ε is a dummy variable representing the vertical coordinate.

The method of solution consists of predicting $\nabla^2\psi$, ψ, u', v', and T from (19), (20), (21), (22), and (6), respectively. The total current is then obtained by adding the vertical shear part to the vertical average part after the latter is obtained from ψ using (17) and (18). The diagnostics ρ, w, and p' are obtained from (5), (16), and (23), respectively.

2.3. Finite Difference Scheme and Resolution

In the horizontal a space-staggered B scheme [*Arakawa and Lamb*, 1977] is used. This scheme gives a superior representation of the geostrophic adjustment process for multilevel models [*Batteen and Han*, 1981]. The horizontal grid spacing is 8 km in the cross-shore direction and 11 km alongshore. This horizontal resolution allows realistic spatial resolution of mesoscale features in the CCS, which have typical wavelengths of the order of 100 km [*Breaker and Mooers*, 1986].

In the vertical there are 10 layers separated by constant z levels of 13, 46, 98, 182, 316, 529, 870, 1416, 2283, and 3656 m. This spacing scheme concentrates more layers in the upper, dynamically active part of the ocean, above the thermocline.

2.4. Domain Size and Boundary Conditions

The model domain for the basic study (Figure 1) extends 12.5° off the west coast of the United States, from 35° to 47.5°N. This covers an area 1408 km in the alongshore direction and 1024 km in the cross-shore direction. The eastern boundary of the model domain is closed, and has both the tangential and cross-shore components of velocity set to zero. As in other wind-forced, process-oriented modeling studies [e.g., *McCreary et al.*, 1991], to isolate the role of wind forcing in the generation of eddies, the eastern boundary is initially modeled as a straight, vertical wall (in a sensitivity study in section 4, the straight coastline will be replaced by irregular coastline geometry), and there are no topographic variations. The constant depth used in the model is 4500 m.

The northern, southern and western borders are open boundaries, which use a modified version of the radiation boundary conditions of *Camerlengo and O'Brien* [1980]. In particular, whether a boundary grid point is treated as an inflow point or as an outflow point for a particular prognostic variable is determined by the sign of a dynamically computed effective group velocity. This group velocity is defined as the ratio of the local time derivative and the local space derivative normal to the boundary. If the boundary grid point is thereby determined to be an inflow point, then the value of the prognostic variable at the boundary grid point is set to its value at the previous time step. If the boundary grid point is determined to be an outflow point, its value is set equal to that of the nearest interior grid point. Some spatial smoothing is also applied within five grid points (~50 km) of the open boundaries.

2.5. Heat and Momentum Diffusion

Because this study is designed to investigate the generation of mesoscale eddies, the type of diffusion used in the model equations is an important issue. Laplacian lateral heat diffusion tends to suppress the formation of mesoscale eddies by diminishing baroclinic signals at that scale, thus making it more difficult for baroclinic instabilities to overcome diffusive damping [*Holland and Batteen*, 1986]. Biharmonic diffusion, on the other hand, tends to allow the formation of mesoscale instabilities because it tends to damp at scales smaller than mesoscale eddies [*Holland*, 1978]. As a result, the use of biharmonic lateral diffusion should allow mesoscale eddy generation via barotropic (horizontal shear) and/or baroclinic (vertical shear) instability mechanisms. For these reasons, biharmonic lateral heat and momentum diffusion are used in the model. Weak vertical eddy viscosities and conductivities are also used. (See Table 1 for the choice of coefficients.)

2.6. Initial Conditions

The initial mean stratification used in all experiments is an exponential temperature profile with a vertical length scale of $h = 450$ m. The exact form is

$$T(z) = T_B + \Delta T e^{z/h}. \tag{24}$$

The approximation assumes $T_B = 2°C$ to be the temperature at great depth. $\Delta T = 13°C$ is the increase in temperature between the bottom of the ocean and the surface. This temperature profile is the same profile used by *Batteen* [1989] and *Batteen et al.* [1989] and was derived by *Blumberg and Mellor* [1987] from available CCS observations of the long-term, mean climatological temperature stratification for the CCS region as a whole.

2.7. Surface Thermal Forcing

To isolate the effects of wind forcing in this process-oriented study, the net heat flux at the sea surface should initially be zero. In this way, any heat flux that is discernible will have been generated by an increase or decrease of sea surface temperature resulting from wind-forcing effects [*Batteen et al.*, 1989]. To accomplish this, an initial air temperature is chosen that forces the net flux of longwave radiation, sensible heat, and latent heat to balance the heating due to solar radiation. This air temperature is then used in the model for all experiments. Any subsequent surface heat flux forcing is therefore a secondary effect of the changes to sea surface temperature due to the wind forcing.

2.8. Wind Forcing

The model is forced from rest with wind fields on a 2.5° by 2.5° grid from the European Centre for Medium-Range Weather Forecasts (ECMWF) "surface" wind analyses [*Trenberth et al.*, 1990], which are 1000-mbar rather than surface analyses. (According to *Trenberth et al.* [1990], the surface and 1000-mbar wind data can be assumed to be the same because ship winds at ECMWF prior to September 1985 were effectively assigned to the 1000-mbar level. Comparisons at ocean weather ship *Lima* showed good agreement between the 1000-mbar and observed wind speeds.) The monthly mean stresses based on twice-daily wind analyses from 1980–1989 have been interpolated spatially to the 8 by 11 km model resolution and temporally to daily wind values. Note that such coarse horizontal spacing in the stresses cannot adequately resolve finer (i.e., less than 2.5°) horizontal scales of the wind field, such as the wind stress curl near the coast.

Figure 2 depicts the seasonal winds starting with January 15 (day 15). The atmospheric pressure pattern for January (Figure 2a) has a low (i.e., the Aleutian Low) to the north and a high (the North Pacific High) to the south, which results in a wind divergence near 40°N. This pattern of poleward winds north of 40°N and equatorward winds to the south continues through February and March. During April (Figure 2b) and May the divergence in the wind field migrates poleward. By June an equatorward component in the wind field is observed along the entire domain. The strongest equatorward winds are discernible from July (Figure 2c) through August. By October (Figure 2d) the winds start to weaken throughout the domain, and a divergence in the wind field is observed in the north. This divergent wind pattern continues through November. By December the wind divergence has returned to ~40°N.

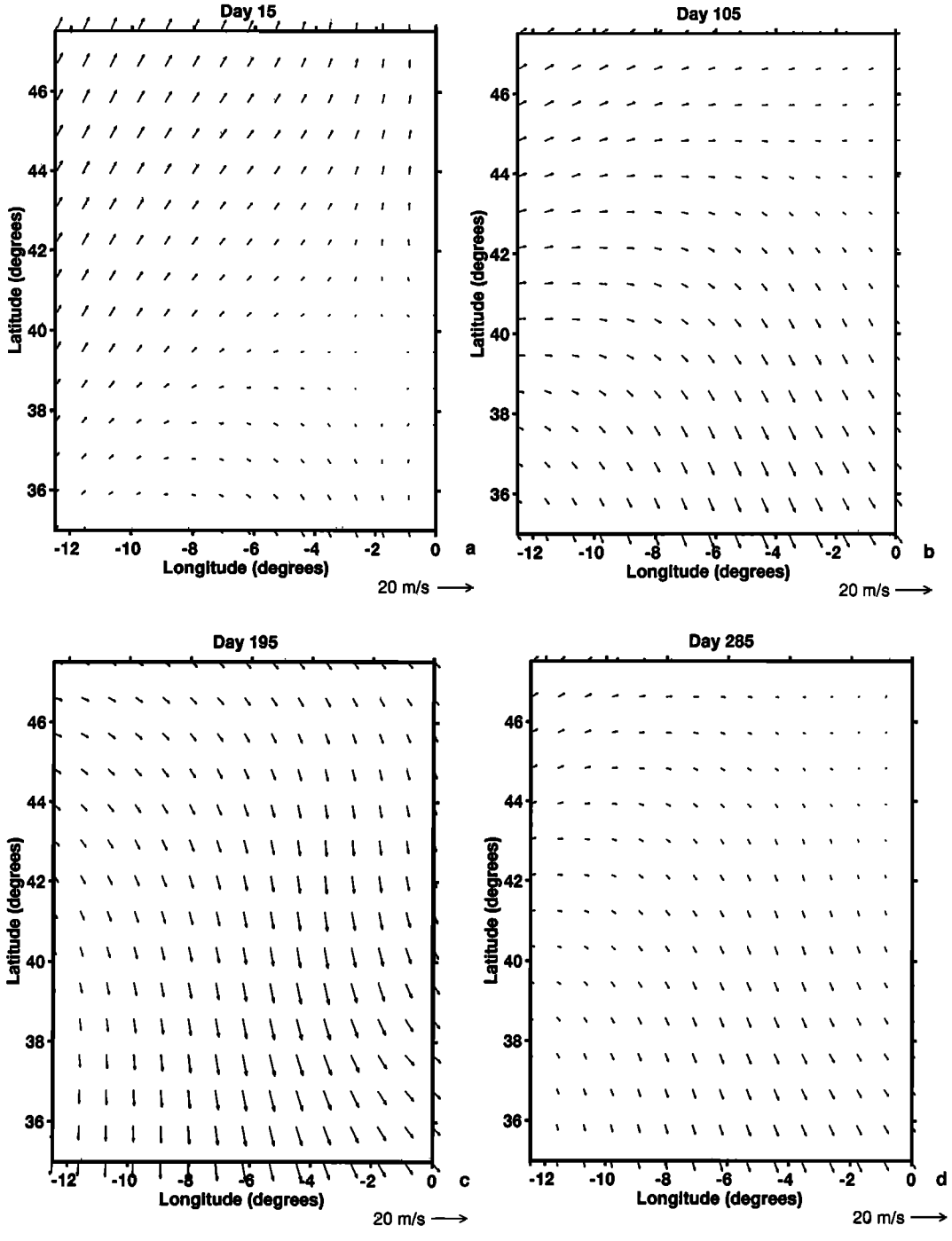

Figure 2. Climatological (1980–1989) ECMWF winds used in experiments 1 and 2 in m/s for (a) January, (b) April, (c) July, and (d) October. Maximum wind vector is 20 m/s.

2.9. Energy Analysis Technique

The energy technique used is the same as that used and described by *Batteen et al.* [1992a] and is based on that of *Han* [1975] and *Semnter and Mintz* [1977]. This analysis is done to gain a better understanding of the types of energy transfer during unstable flow in the CCS. A brief summary of the method follows.

Kinetic energy is calculated for the horizontal components. After a quasi-steady state is reached where the total kinetic energy is nearly constant, mean kinetic energy (MKE) and eddy kinetic energy (EKE) are calculated using the sum of squared mean and horizontal fields, respectively. Next, the available potential energy is calculated and used to determine when a quasi-steady state is reached and when statistics should be collected. Then both mean and eddy available energies are computed. The barotropic and baroclinic energy transfers, defined by *Batteen et al.* [1992a], are used to argue for the type of instability mechanism (e.g., barotropic, baroclinic, or mixed) leading to the initial eddy generation in each experiment.

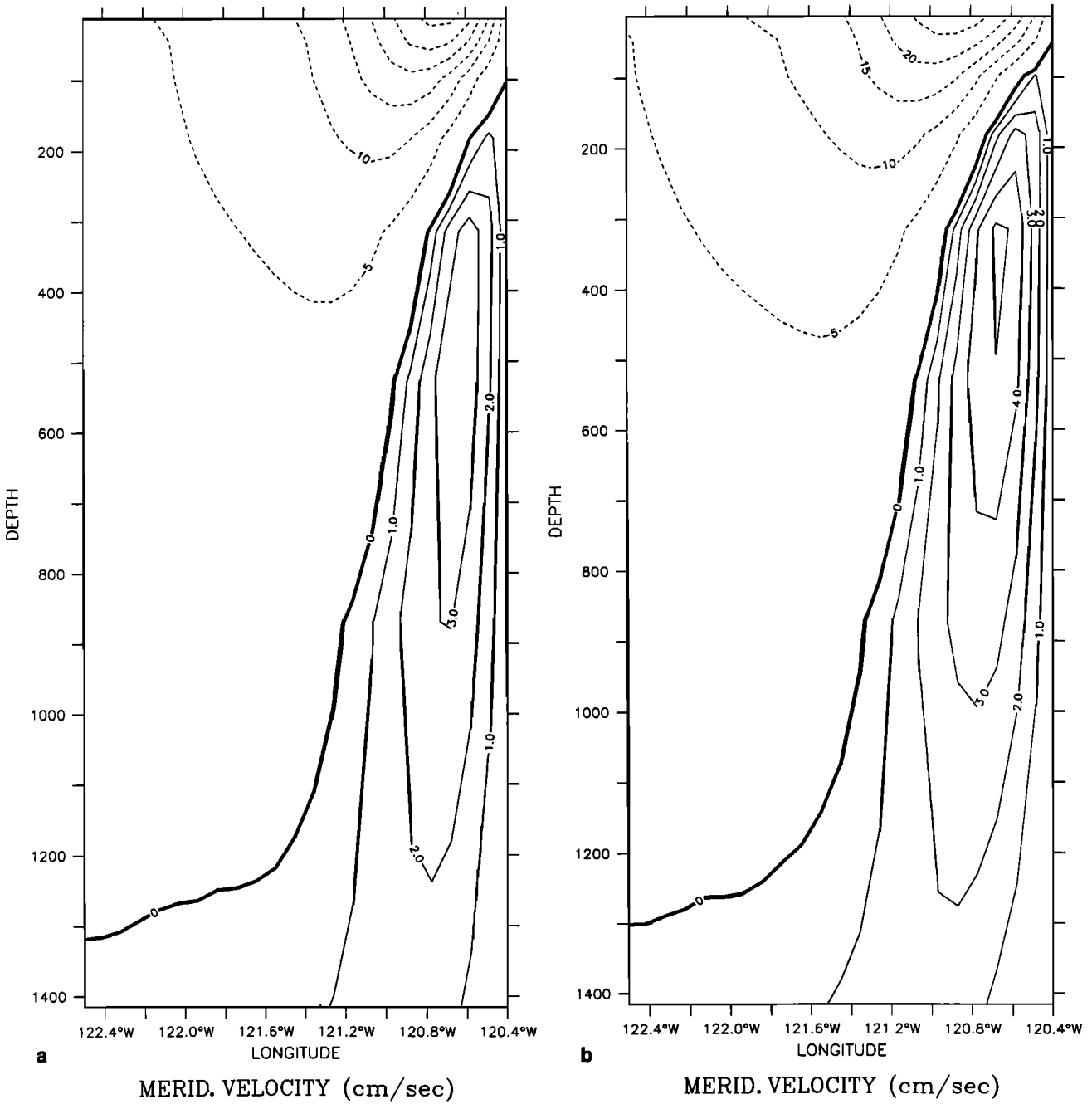

Figure 3. Cross-shore section at 41.3°N of the meridional component of velocity (v) in the coastal region for experiment 1 at days (a) 180 and (b) 210. In all the cross-shore sections of v presented (i.e., Figures 3, 5, 8b, 8c, 10, and 12), solid (dashed) lines indicate poleward (equatorward) flow. The contour interval is 1 cm/s (5 cm/s) for poleward (equatorward) flow. The coast is at 120.4°W.

3. Results of the Basic Study

3.1. Spin-Up Phase

Here we describe the oceanic response to the climatological wind pattern (Figure 2) that is used to force the model from rest. Initially, the solution spins up linearly. In response to the prevailing poleward winds in the north, a poleward coastal surface current of ~3 cm/s develops in the poleward end of the model domain within ~100 km of the coast. After being present for ~45 days, it retreats farther poleward following the migration of the Aleutian Low. As expected, equatorward wind forcing in the south results in an equatorward surface current in the equatorward end of the model domain. By spring, with the arrival of the North Pacific High along the west coast of North America, the current extends all along the coast. A coastal, poleward undercurrent develops below the surface equatorward current, initially in the equatorward end of the model domain, and, during the upwelling season, along the entire coast.

A cross section of meridional velocity (Figure 3a) shows the typical vertical structure of the equatorward coastal jet and

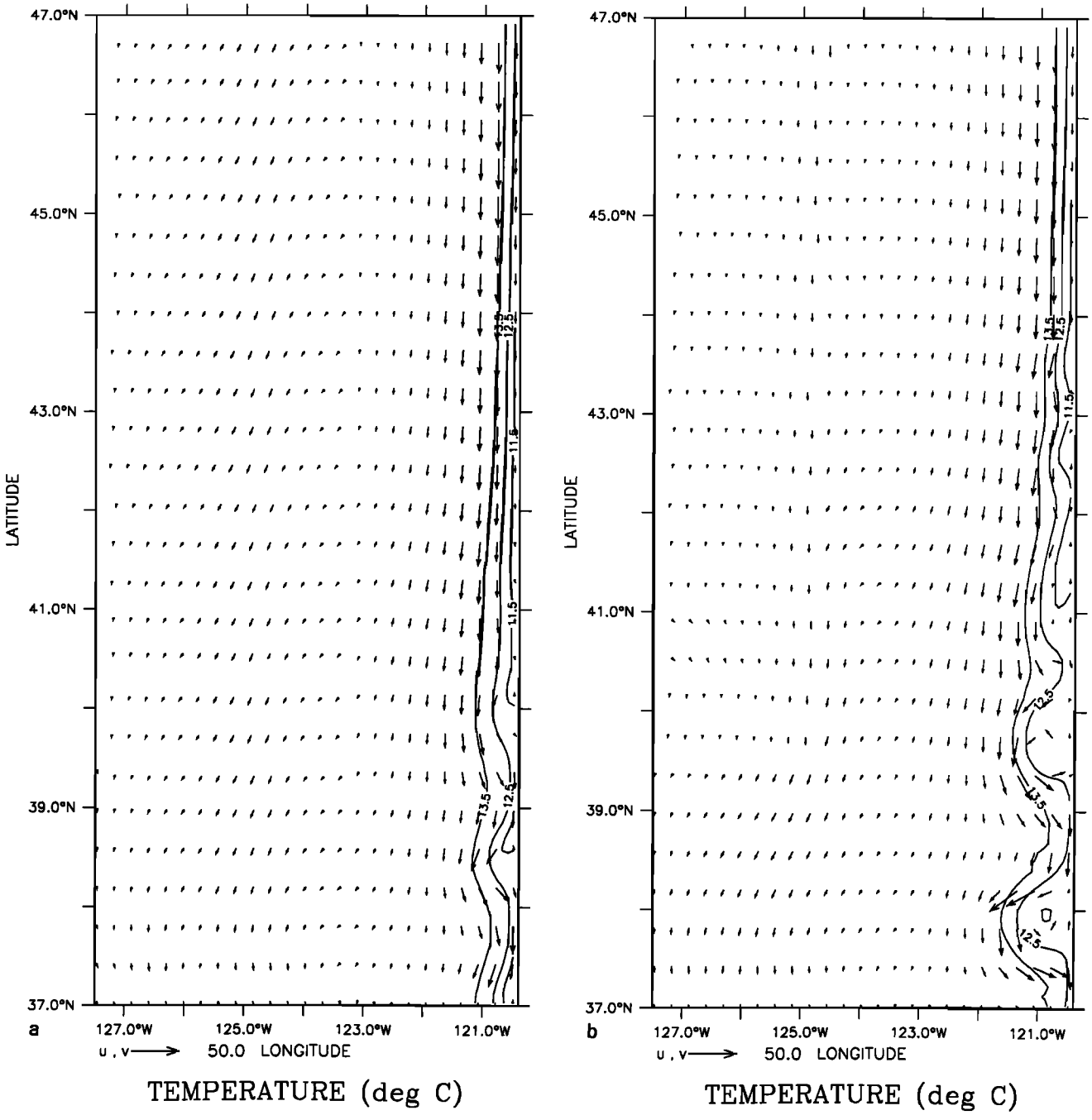

Figure 4. Temperature contours and velocity vectors at 46 m depth in the coastal region for experiment 1 at days (a) 225, (b) 255, (c) 270, (d) 405 (day 40 of year 2), and (e) 540 (day 175 of year 2). The contour interval is 1°C. In all the velocity fields presented (i.e., Figures 4, 7, 8a, 8d, 11, 13, 14, 15a, and 15c), to avoid clutter, velocity vectors are plotted at every third (fourth) grid point in the cross-shore (alongshore) direction. Maximum current velocity is 50 cm/s.

poleward undercurrent during the upwelling season. The coastal jet axis is within ~50 km of the coast and extends from ~100 m depth near the coast to ~200–400 m depth offshore. Core velocities range from ~30 to 40 cm/s. A weaker undercurrent with a core velocity of ~3 cm/s is also seen. The offshore extent of the core of the undercurrent is confined to ~30 km of the coast. Typical core velocities for the undercurrent range from ~3 to 10 cm/s.

As the wind turns equatorward and exerts stress on the water surface, Ekman transport offshore results in the upwelling of cooler water along the coast (for example, see Figure 4a, which shows that the initial conditions of a horizontally uniform temperature field are changed by the presence of colder upwelled water near the coast.). In spring the upwelling is confined to the south, while in summer it is present all along the coast.

As the coastal jet and undercurrent become fully established (for example, see Figure 3b, which shows the structure of the currents just prior to meander formation), the currents become unstable and form meanders (Figure 4a). Cold, upwelling filaments also develop. As the meanders intensify, eddies are

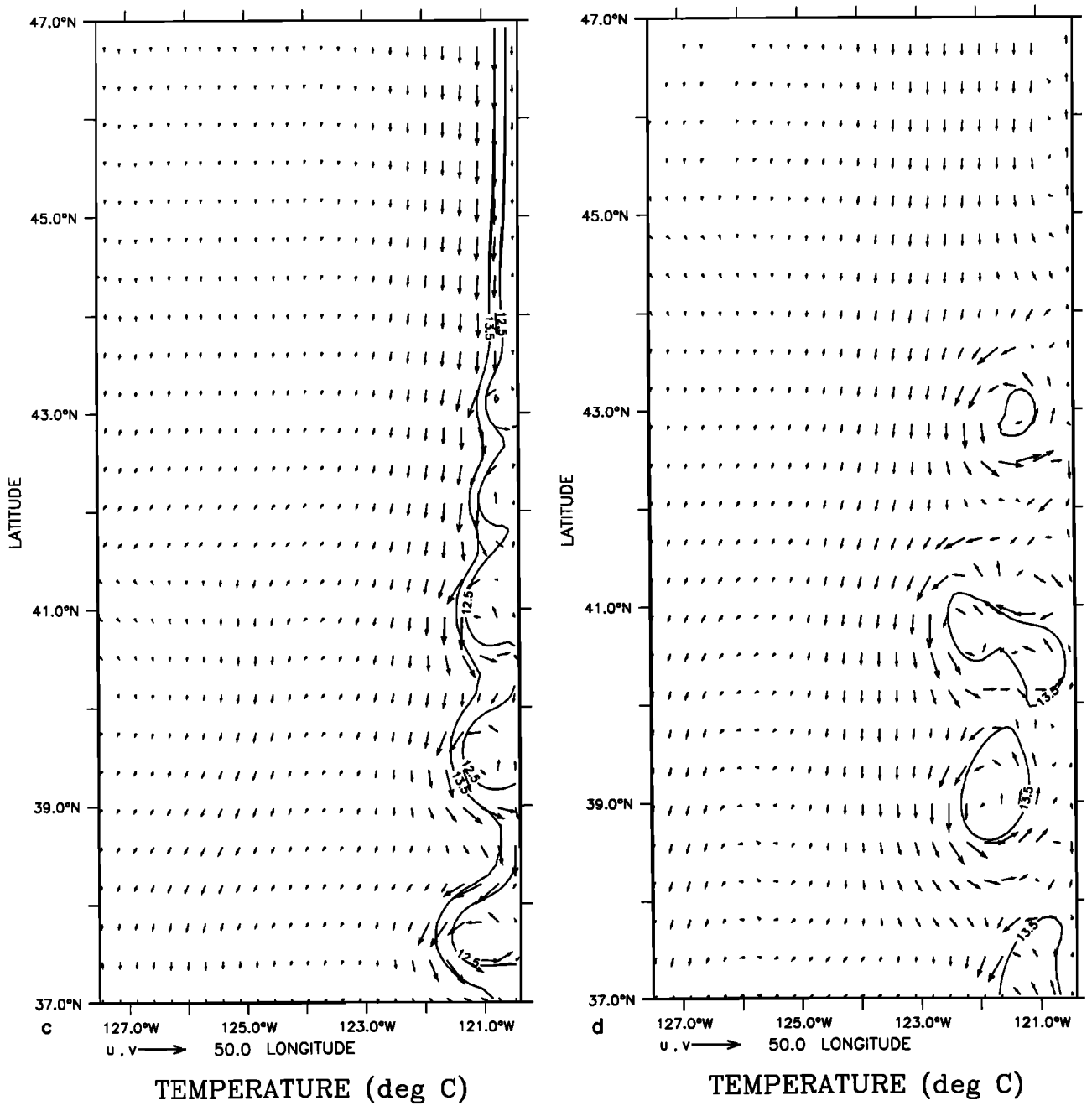

Figure 4. (continued)

formed in the coastal, equatorward region of the domain (e.g., Figures 4b and 4c), due to vertical and horizontal shear instabilities between the equatorward jet and the poleward undercurrent. The eddies are predominantly cold core and cyclonic, $O(100$ km) in diameter, and extend ~50–100 km off the coast. Throughout the summer, which corresponds to the period of maximum equatorward wind stress (e.g., Figure 2c), meanders, filaments, and eddies continue to develop equatorward of ~44°N (e.g., Figure 4c) with alongshore spacings of ~150 km between eddies.

To determine the type of instability that could generate the meander and eddy features, more detailed analysis was performed. Barotropic instability can result from horizontal shear in the currents, while baroclinic instability can result from vertical shear in the currents. As Figures 3a and 3b show, there is considerable horizontal and vertical shear in the upper layer currents. As a result, both types of instability (mixed) can be present simultaneously. Energy transfer calculations, which consist of barotropic (mean kinetic energy to eddy kinetic energy) and baroclinic (mean potential energy to eddy potential energy to eddy kinetic energy) components were performed for the time period (i.e., days 225–255) when the meanders and eddies developed. The results for the instability analysis (not shown) show that both barotropic and baroclinic instabilities are present in the coastal, equatorward region of the domain. As expected, the transfers are strongest in the regions of meander and eddy development.

In fall the cold, upwelled water near the coast disappears

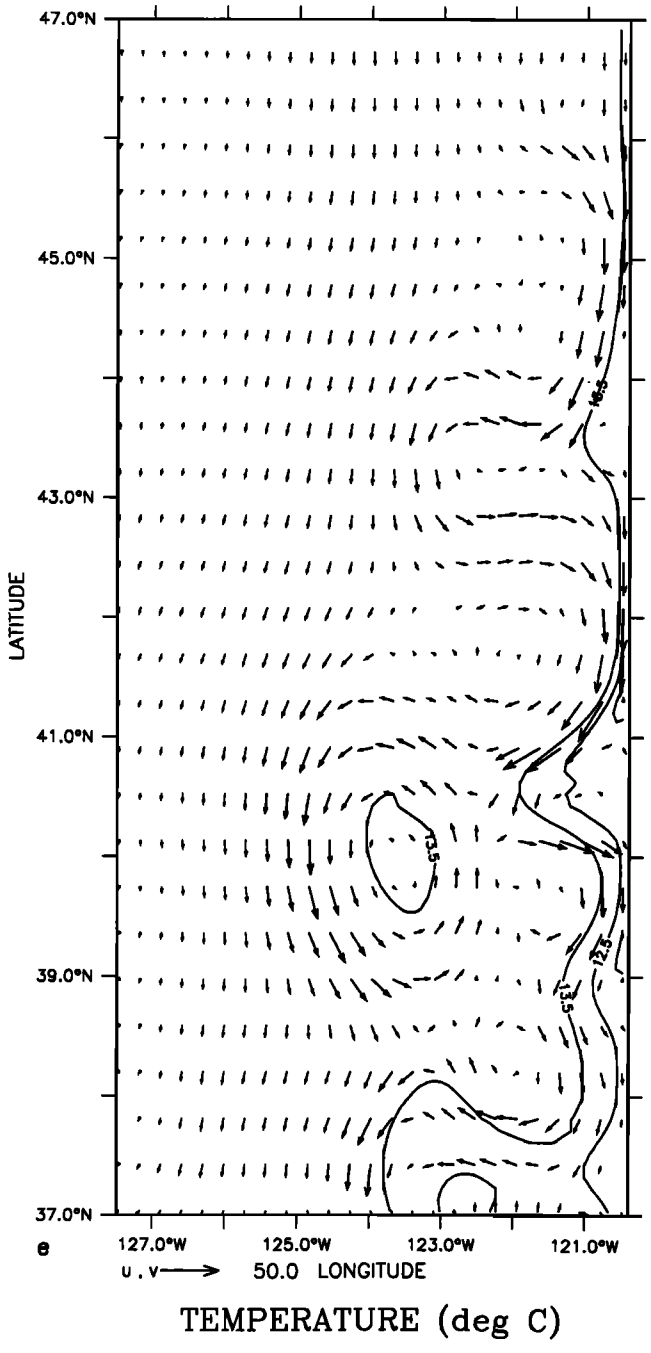

Figure 4. (continued)

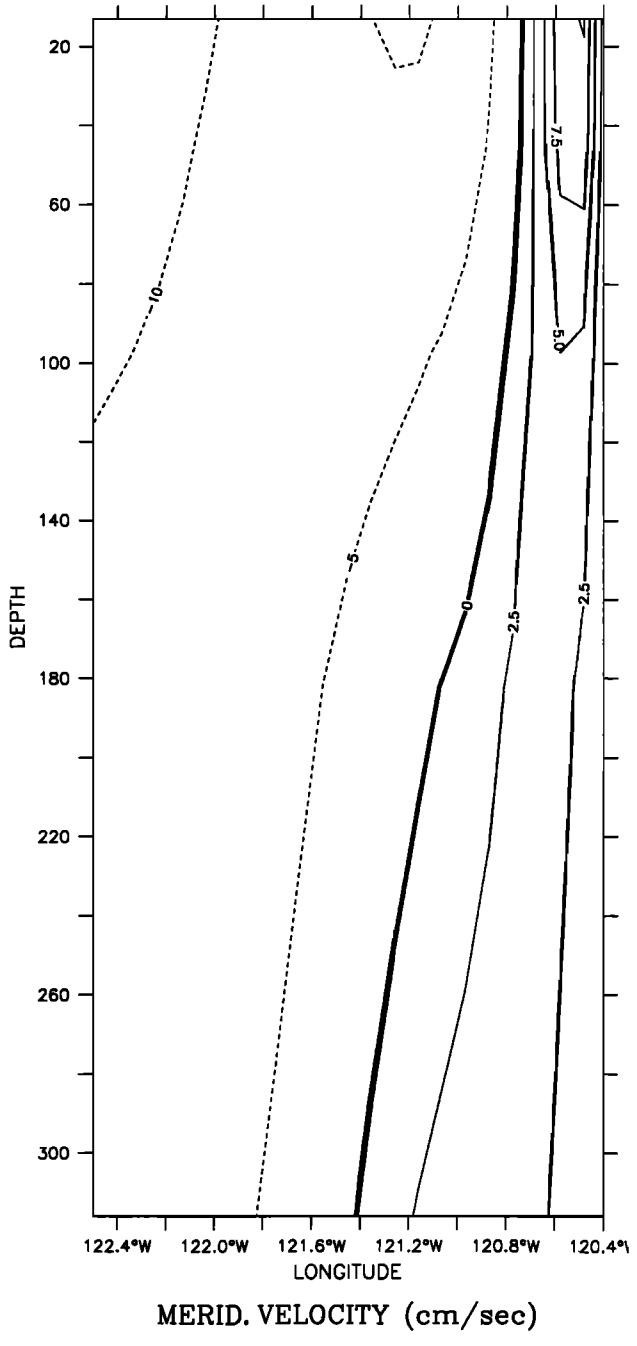

Figure 5. Cross-shore section at 45°N of v in the coastal region for experiment 1 at day 405 (day 40 of year 2). Contour interval is 2.5 cm/s (5 cm/s) for poleward (equatorward) flow.

along with the filaments, first at the poleward end of the model domain and then progressively southward. A surface, poleward current, as at the start of the model simulation, reappears in the poleward end of the model domain close to the coast and remains throughout the winter (e.g., Figures 4d and 5). To the south the offshore equatorward surface current and cyclonic eddies remain present. The equatorward current has taken the form of a meandering jet, with wavelengths of several hundred kilometers, which is embedded with more cyclonic eddies than anticyclonic eddies (e.g., Figure 4d). Throughout the winter, the equatorward jet continues to meander downstream. Since the equatorward jet speeds (~10–30 km/d) are faster than the westward propagating eddy speeds (~5 km/d), the eddies appear to meander both equatorward and westward, as part of the meandering jet.

In spring, with the return of the North Pacific High along the west coast, upwelling of cooler water along the coast redevelops. Inshore of cyclonic meanders of the equatorward jet, upwelling filaments develop. Throughout the upwelling season, cold, cyclonic eddies tend to form offshore of the filaments, while warm, anticyclonic eddies tend to develop downstream of the filaments in regions where the equatorward jet meanders anticyclonically (e.g., Figure 4e). In fall, as expected, the filaments and cold, upwelled water near the coast, disappear. A surface poleward current reappears in the poleward end of the

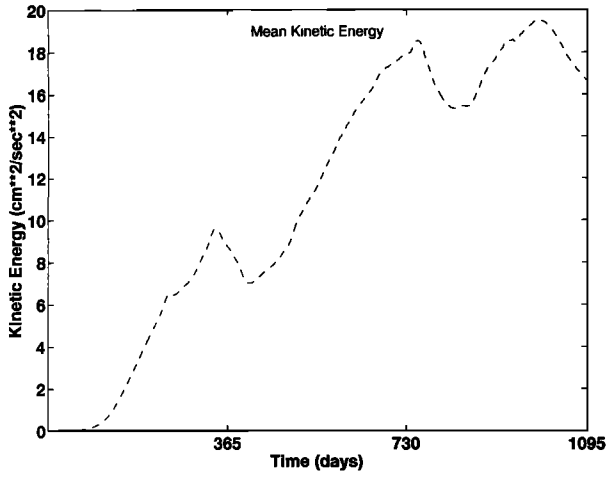

Figure 6. Mean kinetic energy time series for experiment 1 at 46 m depth.

model domain, while to the south, the equatorward jet, embedded with eddies, continues to meander downstream.

Longer experimental runs show that the system has reached a quasi-steady state and that these features continue to be generated and maintained. In particular, the mean kinetic energy has reached a quasi-equilibrium of the annual cycle by the end of 2 years of model simulation time (Figure 6). This quasi-equilibrium is expected, since the source for the mean kinetic energy (i.e., the wind forcing) is seasonal.

3.2. Quasi-Equilibrium Phase

Using year 3 of the longer experimental runs, we time average the model output fields every 3 days for the months of January, April, July, and October to see the seasonal structure of features in the CCS. We use year 3 because Figure 6 clearly shows that a quasi-equilibrium state has been reached by the start of year 3.

The results show that in winter (e.g., Figure 7a) there is an equatorward jet with speeds of ~20 cm/s that meanders both cyclonically and anticyclonically. Strong equatorward flow at the coast occurs only in regions where the jet bends anticyclonically near the coast (e.g., between 40°N and 42°N in Figure 7a). Several cyclonic and anticyclonic eddies of $O(100$ km) diameter are discernible on the offshore side of the jet, while a cyclonic eddy is seen inshore of the jet at ~39°N.

In spring (e.g., Figure 7b), a weak (~10 cm/s) coastal, equatorward current develops south of ~45°N. It flows near the coast until ~41°N, where it veers offshore of the cyclonic eddy at 39°N. The current then joins the stronger (~20–30 cm/s) equatorward jet, which meanders both cyclonically and anticyclonically. The jet has alongshore wavelengths of several hundred kilometers. South of ~43°N, cyclonic eddies of $O(100$ km) diameter are discernible both offshore and inshore of the meandering jet.

In summer (e.g., Figure 7c), upwelling of cooler water is present all along the coast, with evidence of cold, offshore flowing, upwelling filaments at ~44°N, 42.8°N, 41°N, and 39°N, where the coldest water is found. There is both a coastal, equatorward flow present along the coast and an offshore equatorward jet. In areas where the upwelling filaments develop (e.g., south of ~44°N), the coastal current meanders cyclonically and anticyclonically. At ~39°N the coastal current veers offshore of the cyclonic eddy to merge with the meandering jet. The offshore eddy of $O(100$ km) diameter at ~43°N, 125.5°W, is seen to be the same eddy found earlier (i.e., at ~43°N, 124°W, in Figure 7b). The eddy has propagated westward at speeds of ~5 km/d, consistent with Rossby wave propagation speeds.

The results (Figure 8) of averaging the temperature and current fields over the duration of the upwelling season (approximately April through September) shows that an equatorward meandering jet offshore, an equatorward coastal jet inshore, a poleward undercurrent, filaments, and eddies are regular features of the CCS during the upwelling season. The jet meanders both cyclonically and anticyclonically; has alongshore wavelengths of several hundred kilometers, cross-shore excursions of ~100–300 km, and speeds of ~20–30 cm/s; and extends from ~400 to 600 m depth (e.g., Figures 8b and 8c). The coastal current flows near the coast until ~43°N, where it develops meanders of ~150 km wavelength. Between ~39°N and 40°N it veers offshore to merge with the jet. The coastal current has speeds of ~10–30 cm/s and extends from ~100 to 200 m depth (e.g., Figures 8b and 8c). The filaments extend from ~150 km offshore, have widths of ~30–100 km, and extend to ~100 m depth (not shown). The eddies tend to be $O(100$ km) in size and extend to depths of ~400–800 m or deeper (e.g., Figure 8b). Below the coastal current (e.g., Figure 8c) there is a poleward undercurrent, with speeds of ~5 cm/s, which is present all along the coast throughout the upwelling season (e.g., Figure 8d). The undercurrent meanders within ~100 km of the coast. Offshore of the undercurrent are both cyclonic and anticyclonic eddies of $O(100$ km) diameter.

Horizontal maps of the upper layer mean kinetic energy and eddy kinetic energy, averaged over the duration of the upwelling season, are shown in Figures 9a and 9b. Maps of MKE and EKE are suggestive of where the mean and eddy energy sources are to be found [*Holland et al.*, 1983]. A comparison of Figures 8a and 9a shows that high values of MKE are found all along the axis of the offshore equatorward jet, in the coastal regions where the coastal current is strongest, and in the region of the cyclonic eddy offshore of the jet at ~43°N. Maximum values of MKE are found in the region of the strong equatorward jet south of ~40°N, after the coastal current has veered offshore to join the jet.

A comparison of Figures 8a and 9b shows maximum values of EKE south of ~39°N, in the vicinity of the large cyclonic meander of the jet. High values are also found along the axes of the equatorward jet and the coastal current and in the region of the cyclonic eddy at ~43°N, offshore of the jet.

A comparison of Figures 9a and 9b shows that overall, the MKE is larger than the EKE during the upwelling season. This is consistent with the results of the model simulations, which showed that the eddies are generated from instabilities of the mean CC and CUC via baroclinic and/or barotropic instability processes.

After the upwelling season, i.e., in fall (e.g., Figure 7d), the coastal current, south of 45°N, continues to meander cyclonically and anticyclonically and joins the equatorward jet at ~39°N. Several hundred kilometers off the coast, the stronger (~30–40 cm/s) equatorward jet also continues to meander both cyclonically and anticyclonically. The same eddy seen earlier in the upwelling season at ~43°N has continued to propagate westward at speeds of ~5 km/d. The same cyclonic eddy seen earlier at 39°N has also propagated westward at speeds of ~10 km/d.

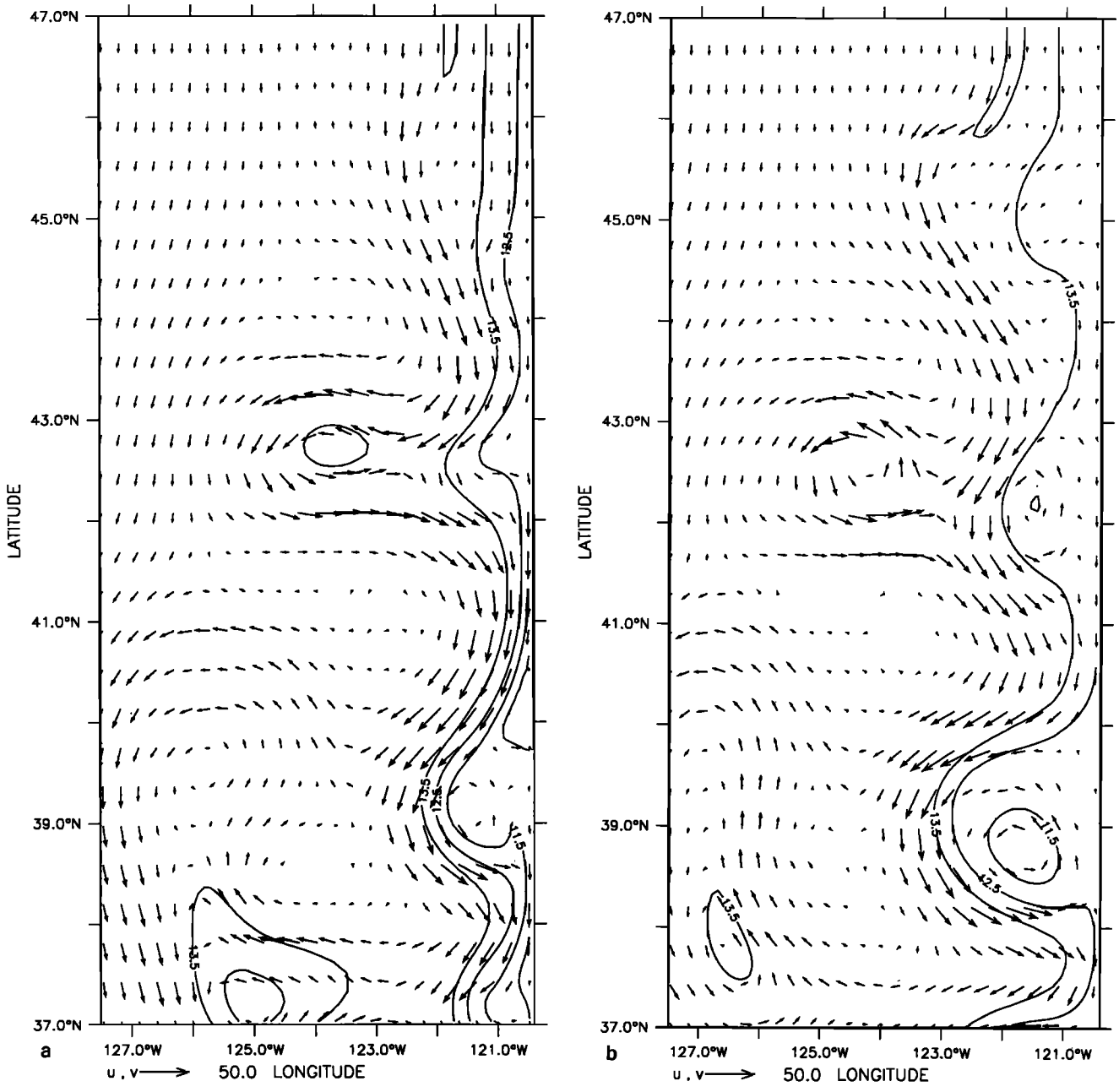

Figure 7. Temperature contours and velocity vectors at 46 m depth in the coastal region for experiment 1 in the third year of model simulation time-averaged over the months of (a) January, (b) April, (c) July, and (d) October. Contour interval is 1°C, maximum velocity vector is 50 cm/s.

On the basis of these results, it is seen that there is a seasonal cycle, as expected from the wind forcing, for the coastal currents, upwelling, and filaments. The meanders and eddies, however, can be quasi-permanent as well as seasonal features. The quasi-permanent features play a significant role in modifying coastal currents, upwelling, and filaments, which leads to large temporal and spatial variability in the CCS.

4. Sensitivity Studies

In a sensitivity study, the results of several numerical experiments are examined to understand the relationship of the generation of the currents, meanders, and eddies on the type of Coriolis parameterization, wind forcing, and coastline geometry used. To facilitate discussion of the results, Table 2 shows the three experiments (including the basic case discussed in the preceding section, which we hereinafter refer to as experiment 1) and the choices for the several parameters.

Like other model sensitivity studies [e.g., *Holland and Lin*, 1975; *Batteen et al.*, 1992b], the basic approach in carrying out these experiments is to change only one parameter for each case. By contrasting the results of each experiment with the results of experiment 1, we gain a better understanding of the importance of each parameter.

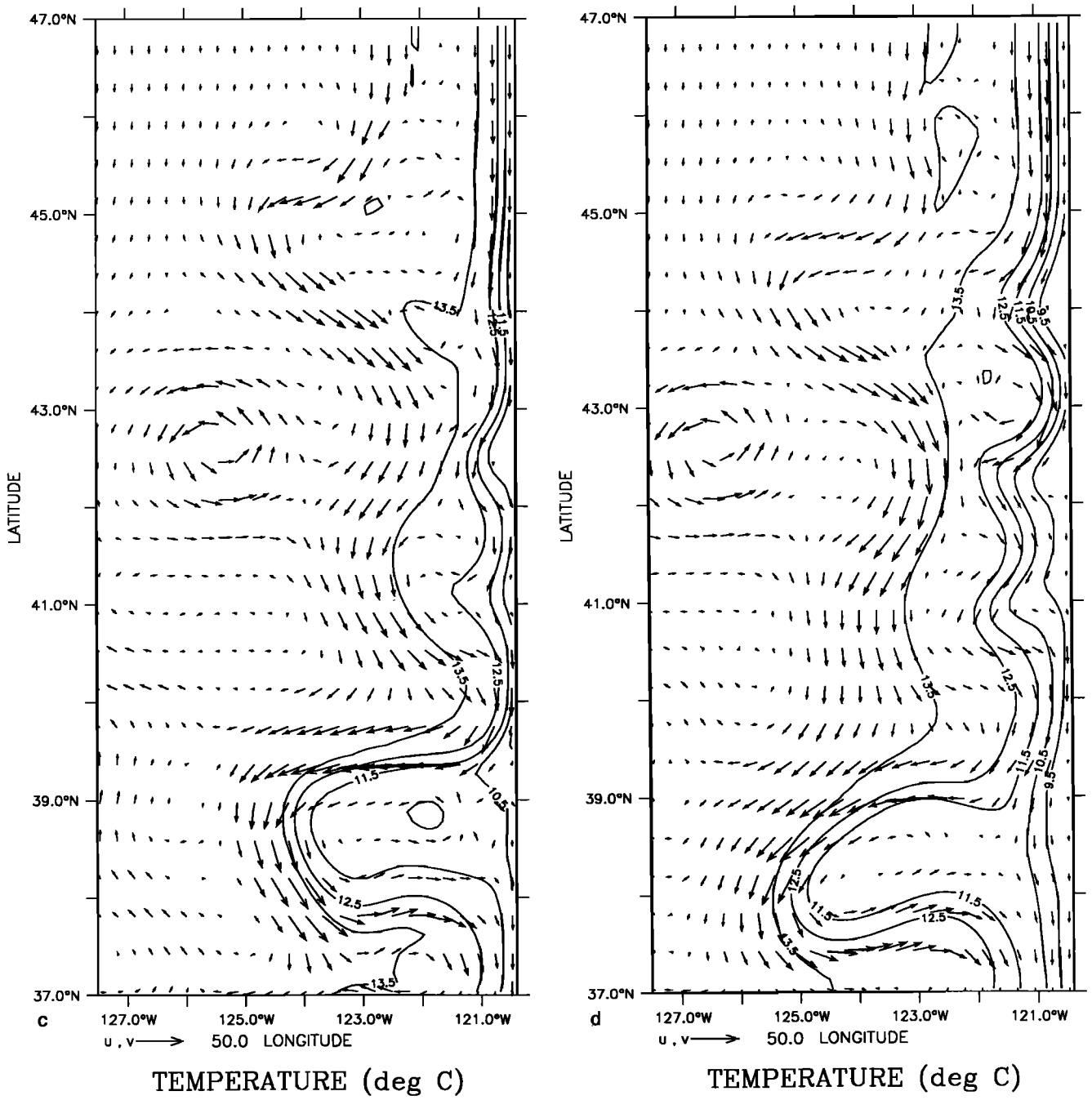

Figure 7. (continued)

4.1. Effect of the Coriolis Parameterization

In experiment 1 a β plane was used. In experiment 2a the effect of an f plane is investigated. All other model parameters are the same as those in experiment 1.

The flow patterns in experiment 2a (Figures 10 and 11) show that a surface equatorward current (referred to as the CC in Table 2) develops that is stronger and deeper than that in experiment 1 (Figures 3 and 4). For example, the core of the CC intensifies to values exceeding 50 cm/s (Figures 10 and 11) compared with those of ~20–40 cm/s (Figure 4 and 5) and deepens to ~500–1500 m depth (Figure 10) compared with ~200–400 m depth in experiment 1 (Figure 3). The poleward undercurrent (referred to as the CUC in Table 2) that forms beneath the CC is much deeper (core depth at ~2000 m or deeper compared with ~200–400 m in experiment 1). Most notably, in contrast to experiment 1, no meanders, eddies, or upwelling filaments develop (for example, compare Figures 4 and 11).

This experiment illustrates the important role that the β effect plays, in the presence of temporal and spatially varying wind fields, in setting up more realistic coastal currents, which subsequently become unstable. The β effect allows the existence of freely propagating waves, i.e., Rossby waves. The offshore propagation of these waves contributes to the generation of an alongshore pressure gradient field, which aids the generation of a realistic undercurrent (i.e., the CUC) along an

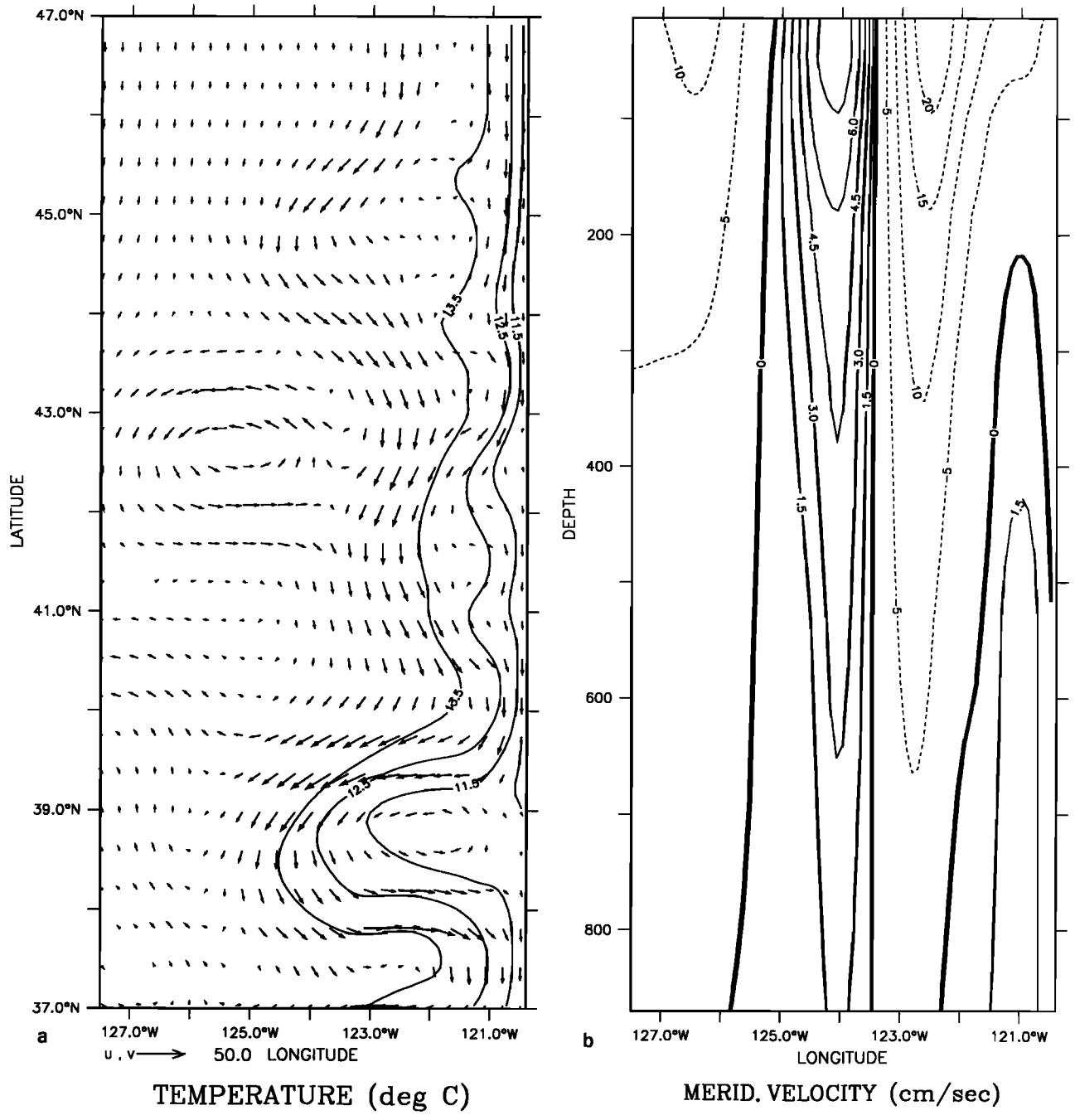

Figure 8. Time-averaged plots for the upwelling season (April–September) for experiment 1 of (a) temperature contours and velocity vectors at 46 m depth, (b) cross section of v at 42.5°N, (c) cross-section of v at 40.5°N, and (d) velocity vectors at 870 m depth. Contour interval is 1°C in Figure 8a and 1.5 cm/s (5 cm/s) for poleward (equatorward) flow in Figures 8b and 8c. Maximum velocity vector is 50 cm/s in Figure 8a and 5 cm/s in Figure 8d.

eastern boundary. (An interesting contrast is that according to *McCreary and Kundu* [1985], along a western boundary, the β effect, in the presence of steady northward (favorable for upwelling) wind-driven flow (with and without curl) prevents an undercurrent from forming beneath the surface current. This is because western boundary Rossby waves propagate in the onshore rather than in the offshore direction.)

As a result, the β effect changes both the vertical and horizontal structures of the currents. In particular, the results of experiment 1 show that as the core of the CUC (which initially lies beneath the CC) intensifies, it shallows and displaces the core of the CC offshore (for example, compare Figures 3a and 3b). As a result, there are strong vertical and horizontal shears in the upper layers between the CC and the CUC. Because this current structure is baroclinically and barotropically unstable, meanders, upwelling filaments, and eddies subsequently develop.

In contrast, the results of experiment 2a show that as the core of the CC (rather than the CUC) intensifies, the core of the CUC deepens (for example, compare Figures 10a and

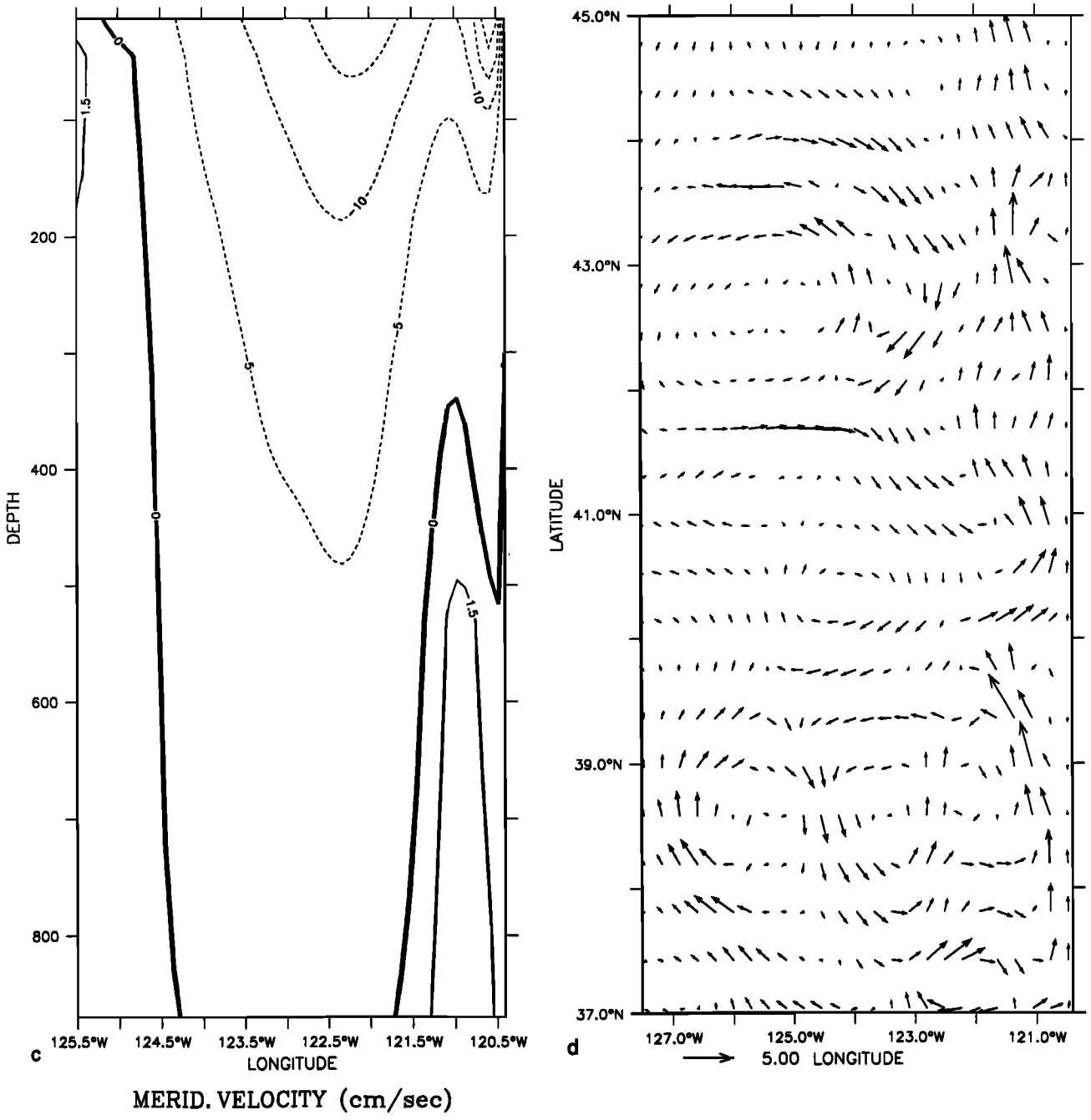

Figure 8. (continued)

10b). As a result, there are no strong vertical and horizontal shears in the upper layers between the CC and the CUC; consequently, no meanders, filaments or eddies develop.

4.2. Effects of Wind Forcing

In previous wind-forcing studies [e.g., *Batteen et al.*, 1989], realistic currents, meanders, and eddies were generated even when an f plane was used. Here we simplify the wind forcing used in experiment 2a to identify the dependence of the generation of the currents, meanders, and eddies in the CCS on the type of wind forcing used.

Since the wind stress is predominantly alongshore in the CCS (Figure 3), in experiment 2b (see Table 2) we first isolate the alongshore component of the wind stress ($\tau^y(x, y, t)$) by setting the cross-shore component ($\tau^x(x, y, t)$) to zero. All other model parameters are the same as those in experiment 2a.

The results are quite similar to those of experiment 2a: i.e., an intensified CC and upwelling develop, the CUC is too deep, and no meanders, filaments, or eddies develop.

Since the CC is generated by the equatorward component of the wind stress, in experiment 2c (see Table 2) we use a constant equatorward wind stress (~1 dyn/cm^2), which is uniform in both the alongshore and cross-shore directions. The results show, as in experiments 2a and 2b, that the CC that develops is too strong and too deep, the CUC that forms beneath the

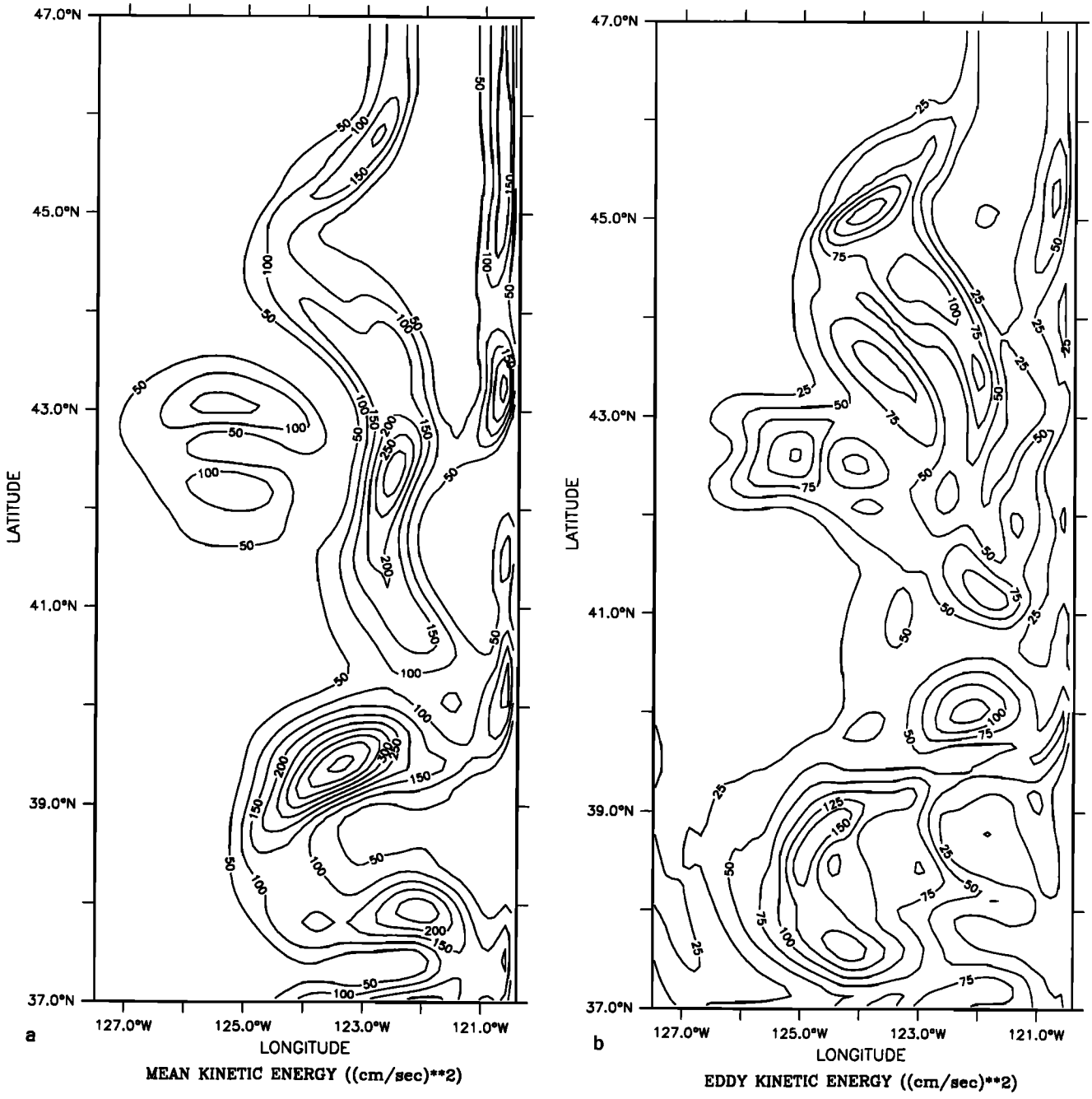

Figure 9. (a) Mean and (b) eddy kinetic energy for experiment 1 at 46 m depth in the coastal region. Contour interval is 50 cm^2/s^2 in Figure 8a and 25 cm^2/s^2 in Figure 8b.

CC is also unrealistically deep, and no meanders, filaments, or eddies are generated.

These results suggest that, on an f plane, in addition to equatorward (upwelling favorable) winds, which result in a surface, equatorward CC, spatial variability in the wind stress is needed to obtain a more realistic CUC. An examination of the cross-shore structure of the equatorward wind field, i.e., $\tau^y(x)$, shows that the wind fields have a predominantly cyclonic wind stress curl structure near the coast (see Figure 2), which, if dominant over the other components of τ^y, would result in poleward flow along the coast. Results from running the model with $\tau^y(x, t)$ only showed results similar to those of experiments 2a and 2b: i.e., an intensified CC and upwelling, a CUC that is too deep, and no meanders, filaments, or eddies.

This leaves the alongshore variability of the wind stress, i.e., $\tau^y(y)$, as the most probable key ingredient for generating a more realistic CUC. To investigate the role of this component of the wind stress, in the last f plane, wind-forcing experiment (experiment 2d in Table 2) we use the same type of equatorward wind forcing as in experiment 2c but impose the forcing only in the interior of the model domain, ~100 km from either the northern or southern boundary. The exact form used is $\tau = \tau_0 Y(y)$, where τ_0 is the wind stress (here equal to 1 dyn/cm^2) and $Y(y)$ is an imposed latitudinal variation that is needed to

Table 2. Types of Coriolis Parameterization, Wind Forcing, and Coastal Geometry for the Experiments Described in Section 4

Experiment	Coriolis Parameterization	Wind Forcing	Coastline Geometry	Result
1	β plane	$\tau(x,y,t)$	straight	basic model: CC, CUC, upwelling, filaments, meanders and eddies present
2a	f plane	$\tau(x,y,t)$	straight	intensified CC and upwelling; CUC too deep; no filaments, meanders, or eddies
2b	f plane	$\tau^y(x,y,t)$	straight	similar to 2a
2c	f plane	τ^y	straight	similar to 2a
2d	f plane	$\tau^y(y)$	straight	similar to 1
3	β plane	$\tau(x,y,t)$	irregular	similar results to 1 but anchoring of upwelling and filaments off capes along with enhanced growth of meanders and eddies off capes

make $\tau = 0$ on the northern and southern boundaries. The wind band forcing function is given by

$$Y(y) = \begin{cases} 1 & 36°\text{N} < y < 47°\text{N} \\ 0 & \text{otherwise} \end{cases}$$

This type of forcing is similar to that used by *Batteen et al.* [1989] and *McCreary et al.* [1991].

The results show that both a CC and a CUC develop, with flow and temperature structures similar to Experiment 1. Upwelling, filaments, meanders, and eddies are generated. The main difference from experiment 1 is that since the wind forcing is equatorward (upwelling favorable) at the onset of the experiment, the currents and eddy features develop and become unstable much earlier (e.g., the currents are unstable as early as day 70 compared with approximately day 210 in experiment 1).

Although this experiment identifies the meridional variation of the alongshore component of the wind stress, i.e., $\tau^y(y)$, as a key ingredient in generating realistic currents, filaments, and eddies in an eastern boundary current regime, this conclusion is valid, on an f plane, only when the wind field is x-independent. When the x dependence of the wind field is included, different results are obtained depending on whether an f plane or β plane is used. On an f plane, as is demonstrated in experiment 2a, the wind field intensifies the CC and deepens and weakens the CUC. In contrast, on a β plane, as is demonstrated by experiment 1, in the presence of primarily equatorward winds, the β effect detensifies the CC and shallows and enhances the CUC. These results identify both the β plane and the meridional variability of the alongshore component of the wind stress as key ingredients for generating currents, filaments, meanders, and eddies in eastern boundary current regimes.

4.3. Effects of Irregular Geometry

In experiment 1 a straight coastline was used. In experiment 3 the effect of irregular coastline geometry is investigated. The same temporal and spatially varying wind forcing is used in experiment 3, except that instead of interpolating the winds to a uniformly straight coastline (Figure 2), the winds are interpolated to irregular coastline geometry north of Monterey Bay. South of Monterey Bay, for a distance of ~100 km, a uniformly straight coastline is used. All other model parameters are the same as those in experiment 1.

The flow and temperature (Figures 12 and 13) patterns in experiment 3 show that a CC and a CUC, with flow structures similar to those in experiment 1, develop. For example, as the core of the CUC intensifies, it shallows and displaces the core of the CC farther offshore (for example, compare Figures 12a and 12b). As a result, there are strong vertical and horizontal shears in the upper layers between the CC and the CUC. Because this current is baroclinically and barotropically unstable, meanders, filaments, and eddies subsequently develop.

In experiment 1, upwelling occurred fairly uniformly along the coast, in conjunction with the arrival of the equatorward CC (e.g., Figure 4a). In contrast, in experiment 3, although the equatorward CC develops fairly uniformly along the coast, the upwelling is relatively patchy. In particular, the coldest, upwelled water is often found at or equatorward of large promontories (e.g., Cape Mendocino in Figures 13a to 13c). Since promontories are areas of the irregular coastline where the alongshore component of the wind stress, τ^y, is at a local maximum, the CC, upwelling, and growth of filaments should be enhanced in these regions during the upwelling season.

The tendency for the cooler water to occur at or equatorward of promontories can be explained as follows. Following *Arthur* [1965], let the (vertical component of) relative vorticity equation be approximated by the horizontal divergence and planetary vorticity terms. Substituting vertical divergence from the continuity equation for horizontal divergence in the vorticity equation and solving for the vertical divergence, we obtain

$$f\partial w/\partial z = D\zeta/Dt + \beta v \tag{25}$$

where the left-hand side (term 1) is the vertical divergence, the first term on the right-hand side (term 2) is the change in relative vorticity, and the second term on the right-hand side (term 3) is the planetary vorticity. Considering the contribution of term 3 to term 1 first, for equatorward flow, term 3 would be less than zero, contributing to upwelling in term 1, while for poleward flow, term 3 would be greater than zero, contributing to downwelling in term 1.

Considering the contribution of term 2 to term 1, in the vicinity of capes, the vorticity can be conveniently determined using natural coordinates as

$$\zeta = V/R_c - \partial V/\partial n \tag{26}$$

where V is the speed, R_c, is the radius of curvature of the streamline, and $\partial V/\partial n$ is the velocity gradient perpendicular to the streamline. By the convention of signs, cyclonic (counterclockwise in the northern hemisphere) flow is taken as positive. Following *Arthur* [1965], we assume that in the vicinity of coastal irregularities, the curvature contribution is more important than the shear contribution. As a result, (26) can be approximated as

$$\zeta = V/R_c$$

Using the above approximation and considering the change in relative vorticity along a streamline near capes for equatorward flow, term 3 in (25) is found to be positive north of capes

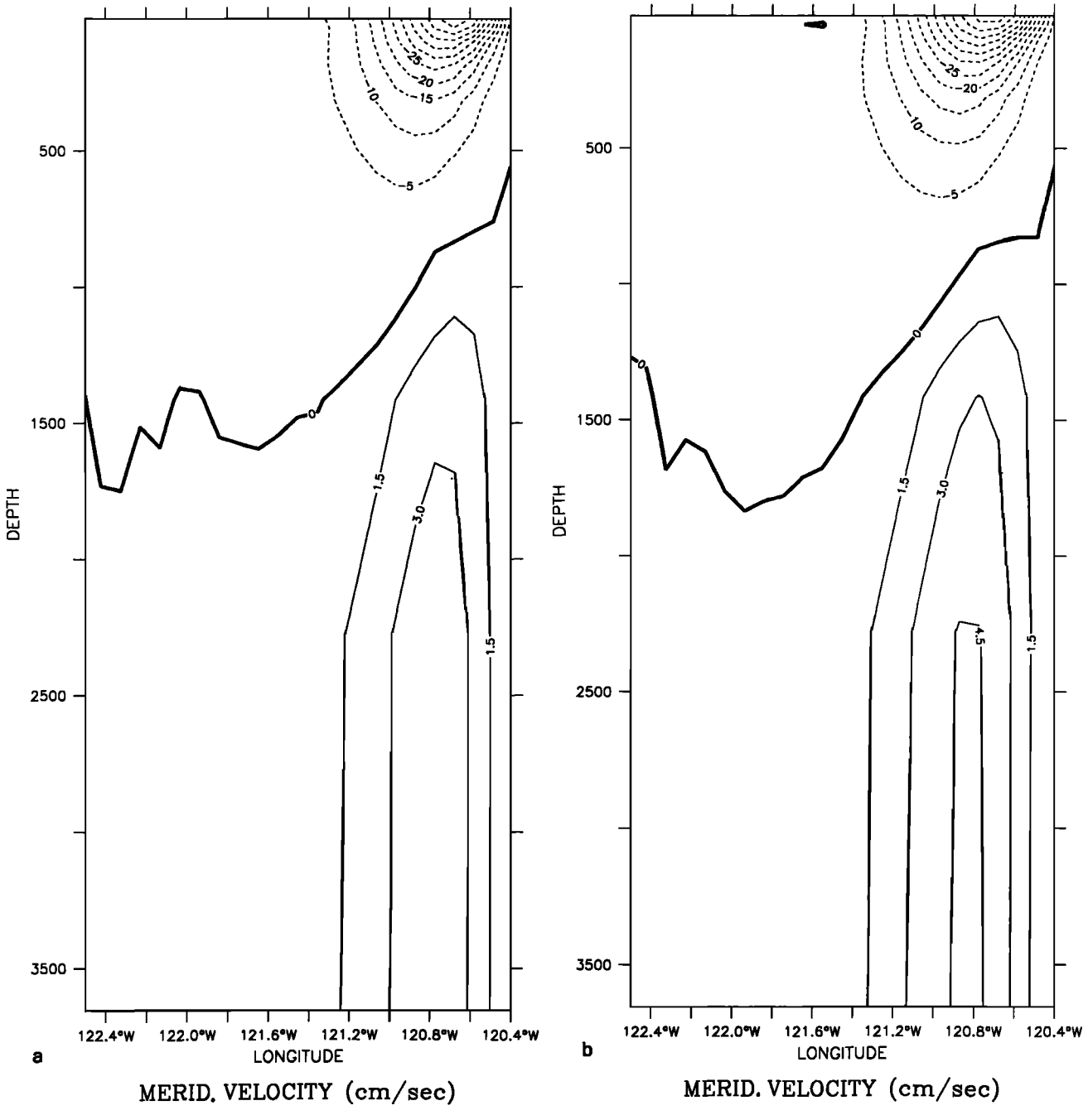

Figure 10. Cross-shore section at 41.3°N of v in the coastal region for experiment 2 at days (a) 180 and (b) 210. Contour interval is 1.5 cm/s (5 cm/s) for poleward (equatorward) flow.

and negative south of capes. Consequently, terms 2 and 3 in (25) will be negative south of capes, contributing to upwelling, while they will have opposite signs north of capes. As a result, when the flow is predominantly equatorward, as in the CCS in the summertime, upwelling should be enhanced south of capes. (Alternatively, when the flow is poleward, both terms are positive north of capes, contributing to downwelling, while south of capes the terms will have opposite signs. As a result, when the flow is poleward, downwelling should be enhanced north of capes.)

In experiment 1 there was no geographical preference for filament formation, meanders, or eddies. In contrast, in experiment 3 the filaments that develop are often "anchored" off of Cape Blanco, Cape Mendocino, and Point Arena (e.g., Figure 13b). Also, in experiment 3 the equatorward CC develops meanders in the vicinity of capes, which intensify and develop into predominantly cyclonic eddies (e.g., Figure 13). In time, these eddies coalesce with other cyclonic eddies to form relatively large (~100–300 km diameter) eddies. After the upwelling season, as in experiment 1, the equatorward CC has taken the form of a meandering jet embedded with several cyclonic eddies (e.g., Figure 13d).

As in experiment 1, longer experimental runs show that the

system has reached a quasi-steady state and that these features continue to be generated and maintained. Using the results of the longer experimental runs (i.e., year 3 of model simulation time), we time average the model output every 3 days for the months of April, July, October, and December to see the seasonal structure of features in the CCS.

The results show that in spring (Figure 14a) and summer (Figure 14b), and throughout the upwelling season (Figure 15a), there is a coastal, equatorward flow with speeds of ~30–80 cm/s that leaves the coast between ~42°N and 43°N, in the vicinity of Cape Blanco, and meanders downstream. The current then takes the form of a meandering jet. The jet has alongshore wavelengths of several hundred kilometers and cross-shore excursions of several hundred kilometers, and it can extend to depths of ~700 m (e.g., Figure 15b). Note the temperature change (i.e., a temperature front) associated with the meander. Inshore of this jet is cooler, upwelled water, while offshore is warmer water and several cyclonic and anticyclonic eddies ranging from ~50 to 200 km diameter, which extend to depths of 200 m or deeper (Figure 15b). South of ~43°N, inshore of the jet, there are both cyclonic and anticyclonic eddies. The cyclonic eddies tend to form in the vicinity of the capes, while the anticyclonic eddies tend to form in the coastal indentations between the capes. A comparison of the spring (Figure 14a) and summer (Figure 14b) velocity and temperature fields shows that as the eddies move westward, they become embedded in the meandering jet.

The results of the lower layer velocity fields, averaged over the upwelling season (Figure 15c) show that there is a coastal poleward undercurrent, with speeds of ~10–20 cm/s, within ~100 km of the coast. Note the shallower depth (e.g., Figure 15b) and the higher speeds of the undercurrent in this experiment compared with experiment 1 (for example, compare Figures 8b and 8d with Figures 15b and 15c). The features in experiment 3 seem more consistent with available CUC observations [e.g., *Huyer et al.*, 1991] than are those in experiment 1. Offshore of the undercurrent are both cyclonic and anticyclonic eddies of O(100 km) diameter.

Horizontal maps of the upper layer MKE and EKE, averaged over the duration of the upwelling season, are shown in Figures 16a and 16b, respectively. A comparison of Figures 15a and 16a shows that the largest values of MKE are found in the region of the strong equatorward jet. High values are also found in the vicinity of the anticyclonic and cyclonic eddies between ~45°N and 41°N.

A comparison of Figures 15a and 16b shows that maximum values of EKE are found along the coast from ~44°N to 41°N, in the vicinity of Cape Blanco, and offshore south of ~39°N. High values are also found from ~124°W to 130°W between 44°N and 41°N. A comparison of Figures 15a and 16b shows that this is where both cyclonic and anticyclonic eddies form. High values of EKE are also found offshore and downstream of Cape Mendocino and Point Arena. The regions where the EKE values are highest, as in the vicinity of Cape Blanco, can be interpreted as areas where eddies are likely to be generated throughout the upwelling season. A comparison of Figures 9b and 16b shows that the EKE values in this experiment are much larger (~5 times) than those in experiment 1 and extend farther offshore.

After the upwelling season, i.e., in fall (e.g., Figure 14c), a poleward flow, with speeds of ~10–20 cm/s, develops within ~100 km of the coast and subsequently replaces the coastal, equatorward flow. Offshore of the poleward flow are several cyclonic eddies. Farther offshore, there is a relatively strong (~50 cm/s) equatorward, meandering jet embedded with both cyclonic and anticyclonic eddies.

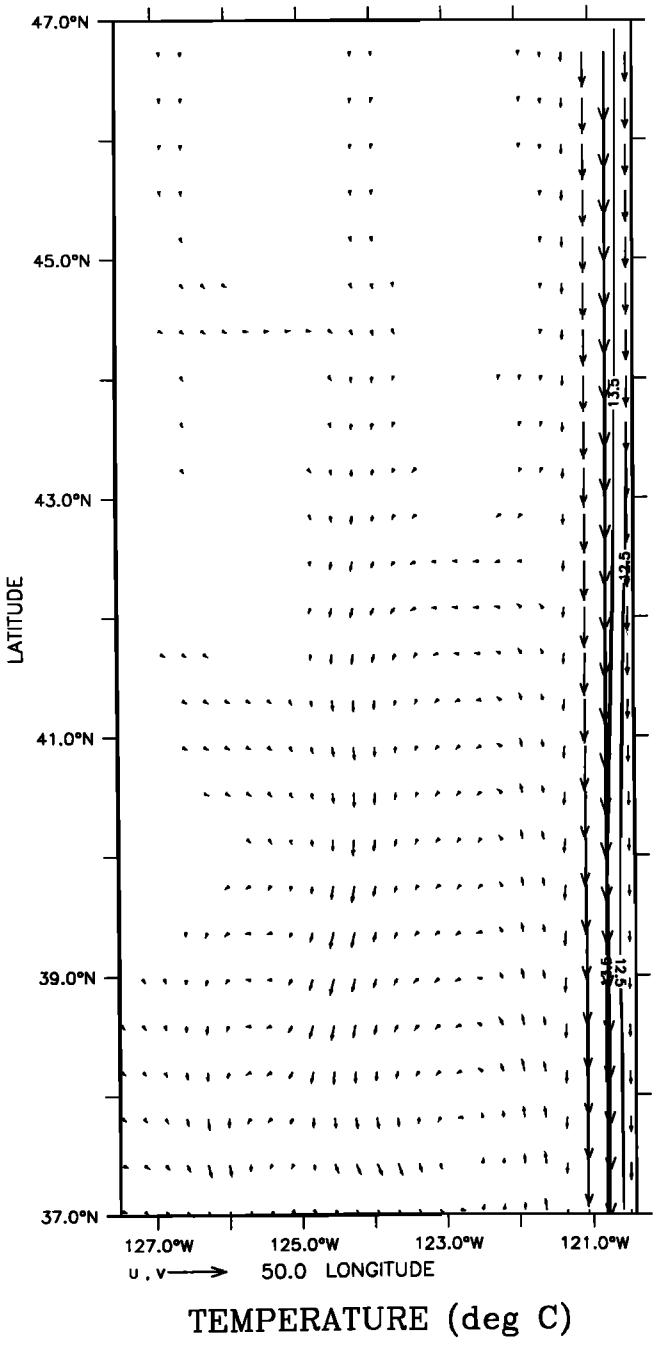

Figure 11. Temperature contours and velocity vectors at 46 m depth in the coastal region for experiment 2 at day 255. Contour interval is 1°C, maximum velocity vector is 50 cm/s.

In the winter (e.g., Figure 14d), in the poleward region of the model domain, the meandering jet has been displaced farther offshore by the westward propagation of cyclonic eddies. In the equatorward part of the model domain, the jet meanders closer to shore, i.e., from ~128°W at 41°N to ~125°W at 38°N. Offshore and inshore of the jet, both cyclonic and anticyclonic eddies fill much of the model domain. A relatively strong

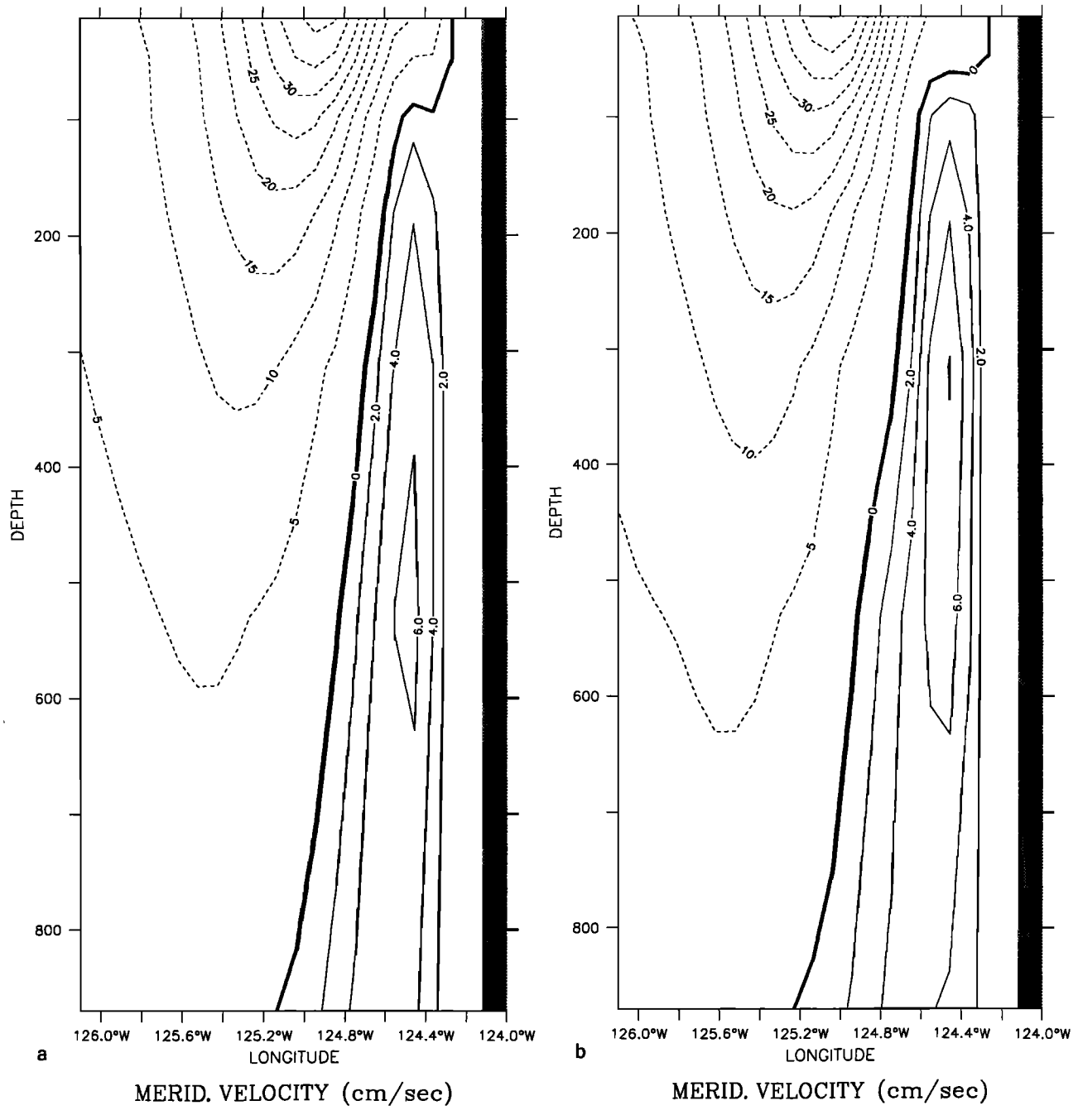

Figure 12. Cross-shore section at 41.3°N of v in the coastal region for experiment 3 at days (a) 180 and (b) 195. Contour interval is 2 cm/s (5 cm/s) for poleward (equatorward) flow.

surface poleward flow near the coast is still present north of ~41°N.

This experiment identifies irregularities in the coastline geometry as key elements for "anchoring" upwelling and filaments and for enhancing the growth of meanders and eddies. The cyclonic eddies tend to form in the vicinity of the capes, while anticyclonic eddies tend to form in the coastal indentations between the capes. This experiment also identifies the region off Cape Blanco as the location where the coastal equatorward flow leaves the coast and forms a jet that develops meanders along a temperature front off California.

5. Summary and Discussion

In section 1 we hypothesized that wind forcing may be the most important mechanism for the generation of the currents as well as for the intense and complex meander, eddy, jet, and filament structures in the CCS. In particular, we stated that the wind forcing can set up the coastal currents, which can subsequently become unstable and lead to the formation of many of the observed features in the CCS.

To investigate this hypothesis, the model was forced from rest with full spatial and temporally varying winds. The results

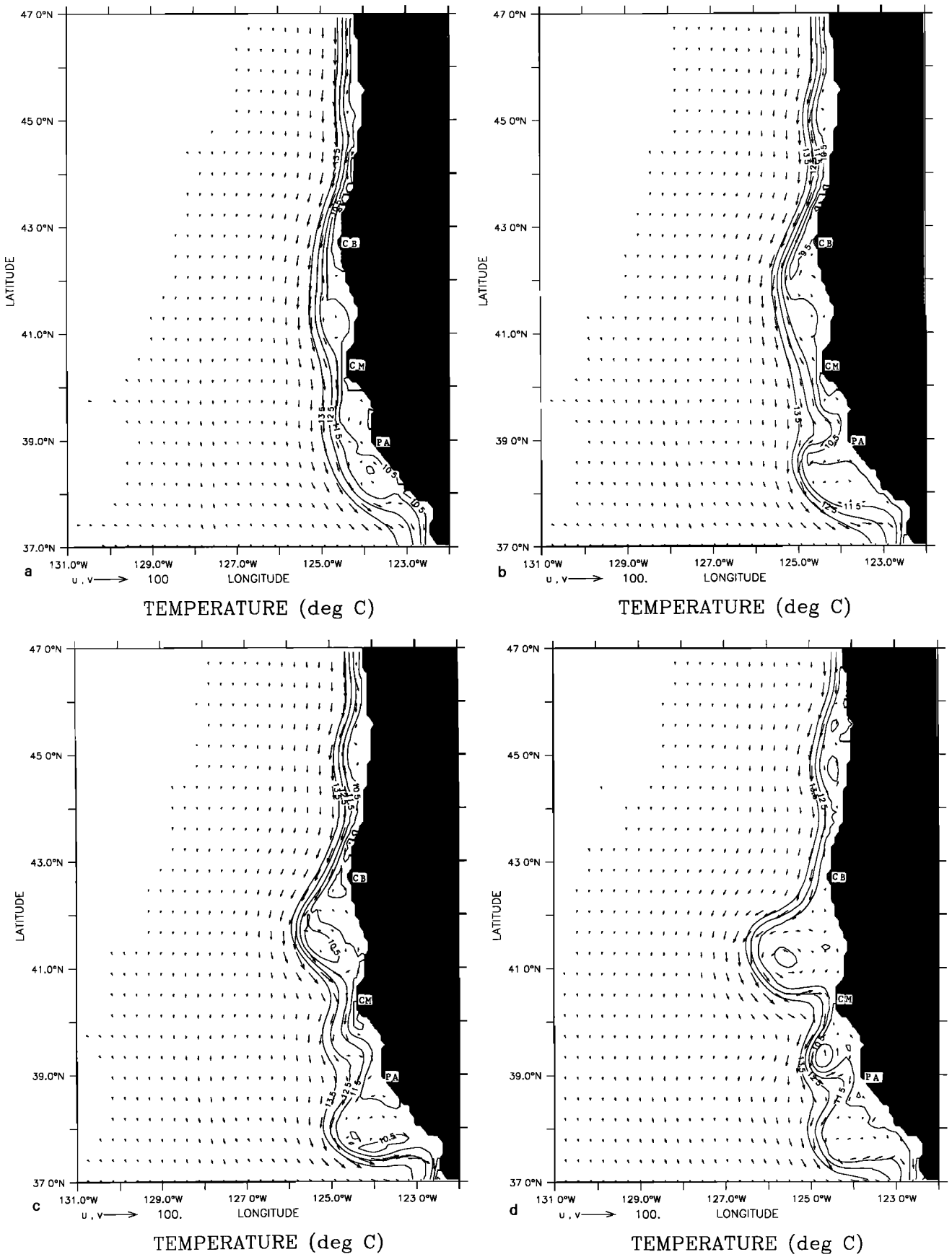

Figure 13. Temperature contours and velocity vectors at 46 m depth for experiment 3 at days (a) 225, (b) 255, (c) 270, and (d) 315. Contour interval is 1°C, maximum velocity vector is 100 cm/s. Here and in the following figures, CB refers to Cape Blanco, CM to Cape Mendocino, and PA to Point Arena.

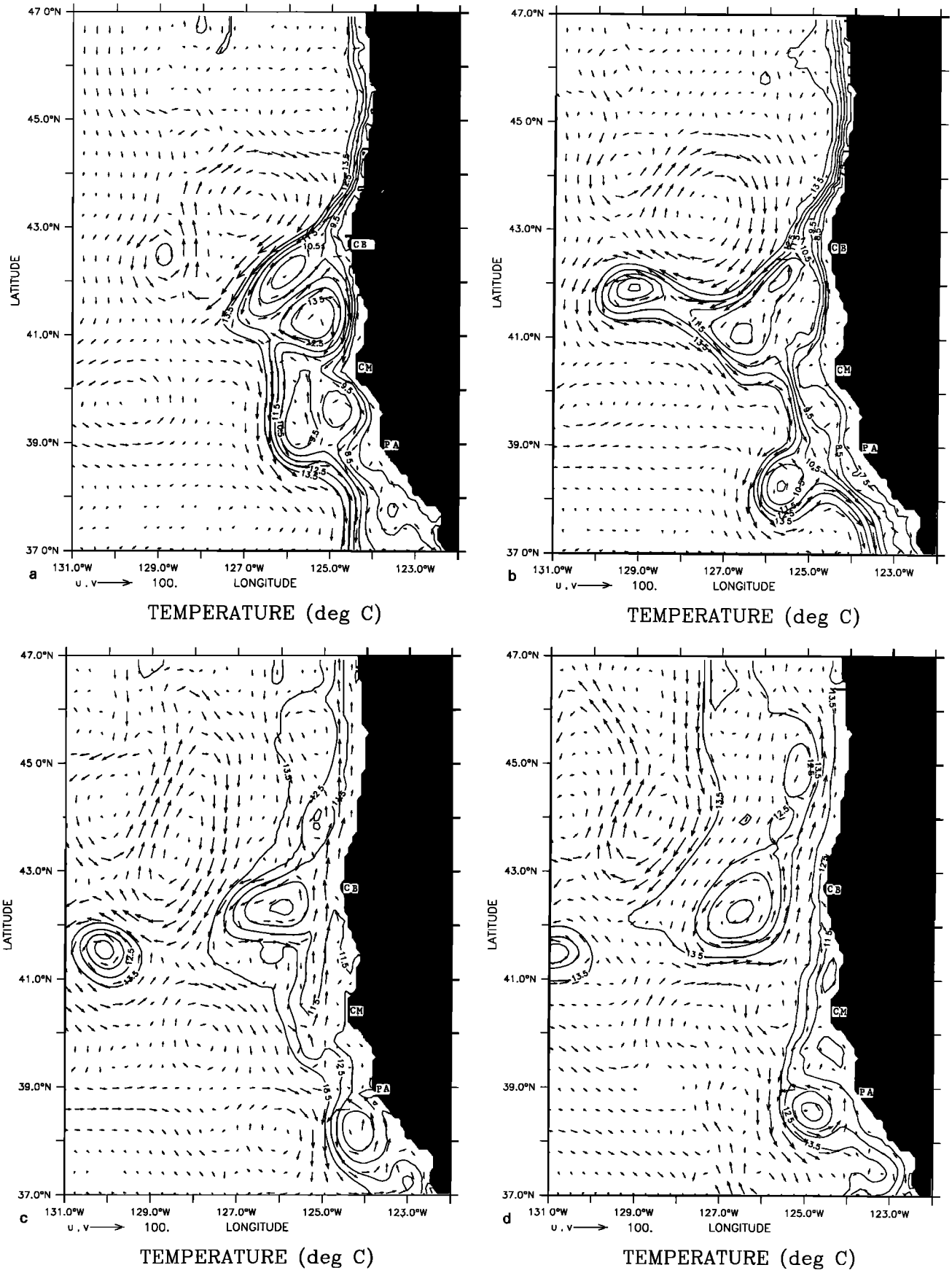

Figure 14. Temperature and velocity vectors at 46 m depth for experiment 3 in the third year of model simulation time averaged over the months of (a) April, (b) July, (c) October, and (d) December. Contour interval is 1°C; maximum velocity vector is 100 cm/s.

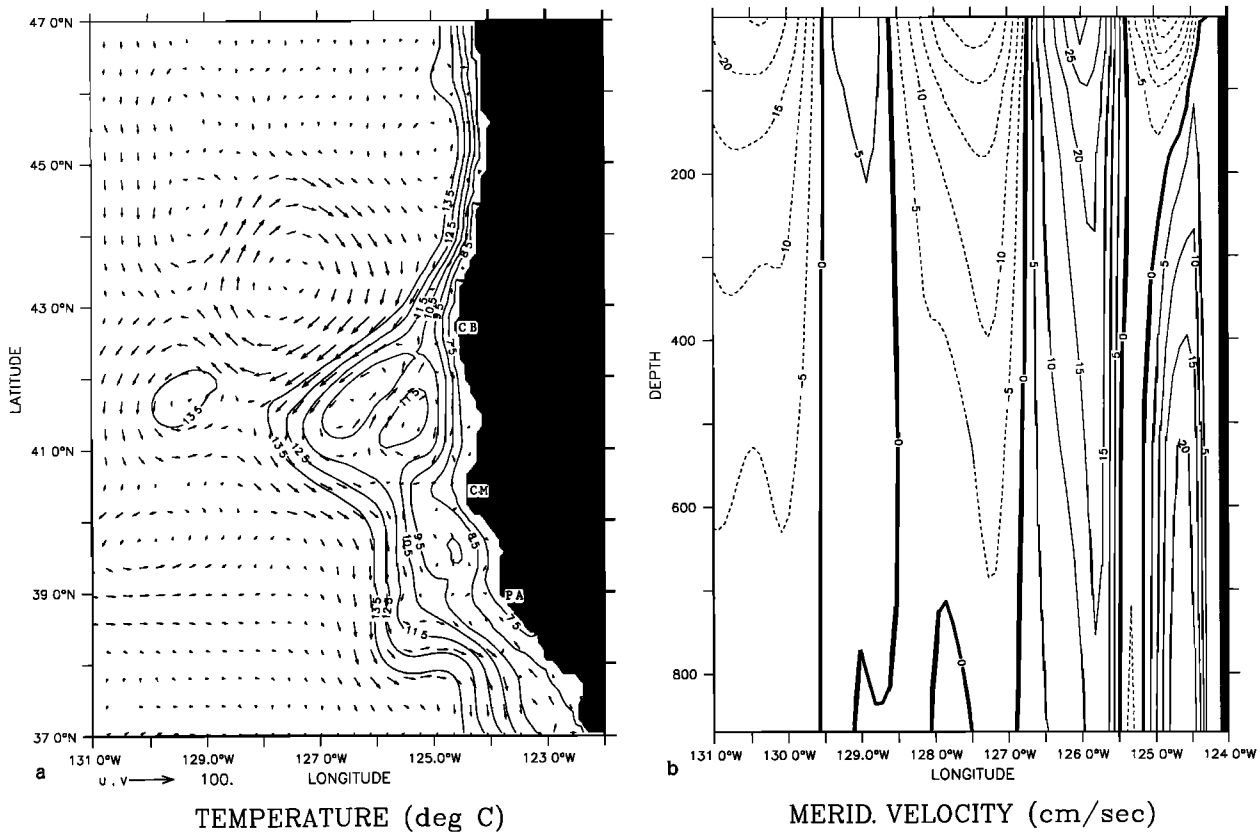

Figure 15. Time-averaged plots for the upwelling season for Experiment 3 of (a) temperature contours and velocity vectors at 46 m depth, (b) cross-section of v at 41.3°N, and (c) velocity vectors at 316 m depth. Contour interval is 1°C in Figure 15a and 5 cm/s in Figure 15b. Maximum velocity vector is 100 cm/s in Figure 15a and 80 cm/s in Figure 15c.

demonstrated that the wind forcing can set up both a CC and a CUC in the upper layers. Since there is both horizontal and vertical shear between the CC and the CUC that are generated, the currents become unstable (via baroclinic and barotropic processes) and lead to the development of meanders, eddies, jets, and filaments.

The temporal nature of the winds demonstrated that, as expected, there is a seasonal cycle for the coastal currents, upwelling, and filaments. In particular, during the upwelling season, a surface coastal, equatorward current overlying a poleward undercurrent develop, while in fall and winter a surface poleward current forms in the poleward end of the model domain. The meanders and eddies were demonstrated to be seasonal as well as quasi-permanent features. The quasi-permanent meandering jet and eddies played a significant role in modifying the coastal current, upwelling, and filaments as they seasonally developed. This led to large temporal and spatial variability in the CCS.

Examining the spatial structure of the wind forcing, it was shown that the meridional variability of the winds was a key ingredient in generating realistic vertical and horizontal structures for the CC and the CUC. An examination of the type of Coriolis parameterization used showed that the β plane also played an important role in generating realistic vertical and horizontal structures of the CC and the CUC. With such structures the currents were baroclinically and barotropically unstable, resulting in the generation of meanders, filaments, and eddies.

Irregularities in the coastline geometry were shown to be important for anchoring upwelling and filaments as well as for enhancing the growth of meanders and eddies. The cyclonic eddies tended to form in the vicinity of capes, while the anticyclonic eddies tended to form in the coastal indentations between the capes. The equatorward current that developed during the upwelling season was also shown to flow along the coast until it reached the vicinity of Cape Blanco, where it veered offshore and formed meanders along a temperature front off California. In fall a surface poleward flow appeared within ~100 km of the coast, replacing the surface coastal, equatorward flow.

Since the last experiment (i.e., experiment 3) incorporated spatial and temporally varying winds as well as irregular coastline geometry and the β plane parameterization, it is useful to qualitatively compare the results of the model simulations with observational data. Since these studies are not model hindcasts but are idealized process-oriented studies, we cannot make direct comparisons with data; however, we can investigate whether the phenomenonological model behavior is qualitatively similar to observational data in the CCS.

Since *Strub and James* [1995] (hereinafter referred to as SJ95) have most recently shown observational results on the large-scale circulation of the CCS during the upwelling season,

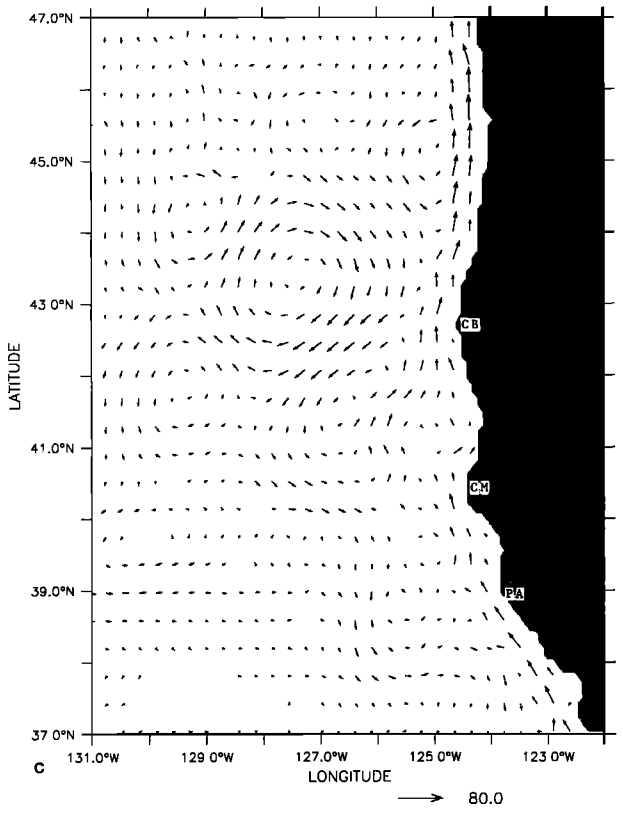

Figure 15. (continued)

we qualitatively compare some of the results of our model simulations with their observations. Let us first compare the results of our July model simulation (Figure 14b) with the SJ95 July observations [SJ95, Figure 2a]. Both SJ95 and our results show the presence of a coastal, equatorward flow leaving the coast in the vicinity of Cape Blanco. Offshore of the jet is a relatively large anticyclonic eddy extending from ~42°N to ~44°N between ~126°W and 128°W. Downstream from Cape Blanco, both SJ95 and our results show the equatorward jet meandering cyclonically offshore and then anticyclonically nearshore, in the vicinity of Cape Mendocino. The jet then veers offshore north of Point Arena and develops a cyclonic meander. Both SJ95 and our results show a band of cooler water of ~7°C along the coast from Cape Blanco and southward along much of the coast, and an equatorward jet separating colder, inshore water from warmer, offshore water. This latter feature is also present in the springtime observations [SJ95, Figure 2a] and model simulations (e.g., Figure 14a). Finally, SJ95 and our results show that there is a connection between the equatorward flow off Oregon and the jet that meanders along a temperature front off California. In particular, the equatorward flow off Oregon and the meandering jet are part of a continuous flow that originates from farther north.

Extending beyond the spring and summer observations of SJ95 to other times of the year when observations tend to be sparse for the large-scale circulation of the CCS, the results of our model simulations suggest that the development of the Davidson Current (e.g., Figure 14c) in fall leads to a separation

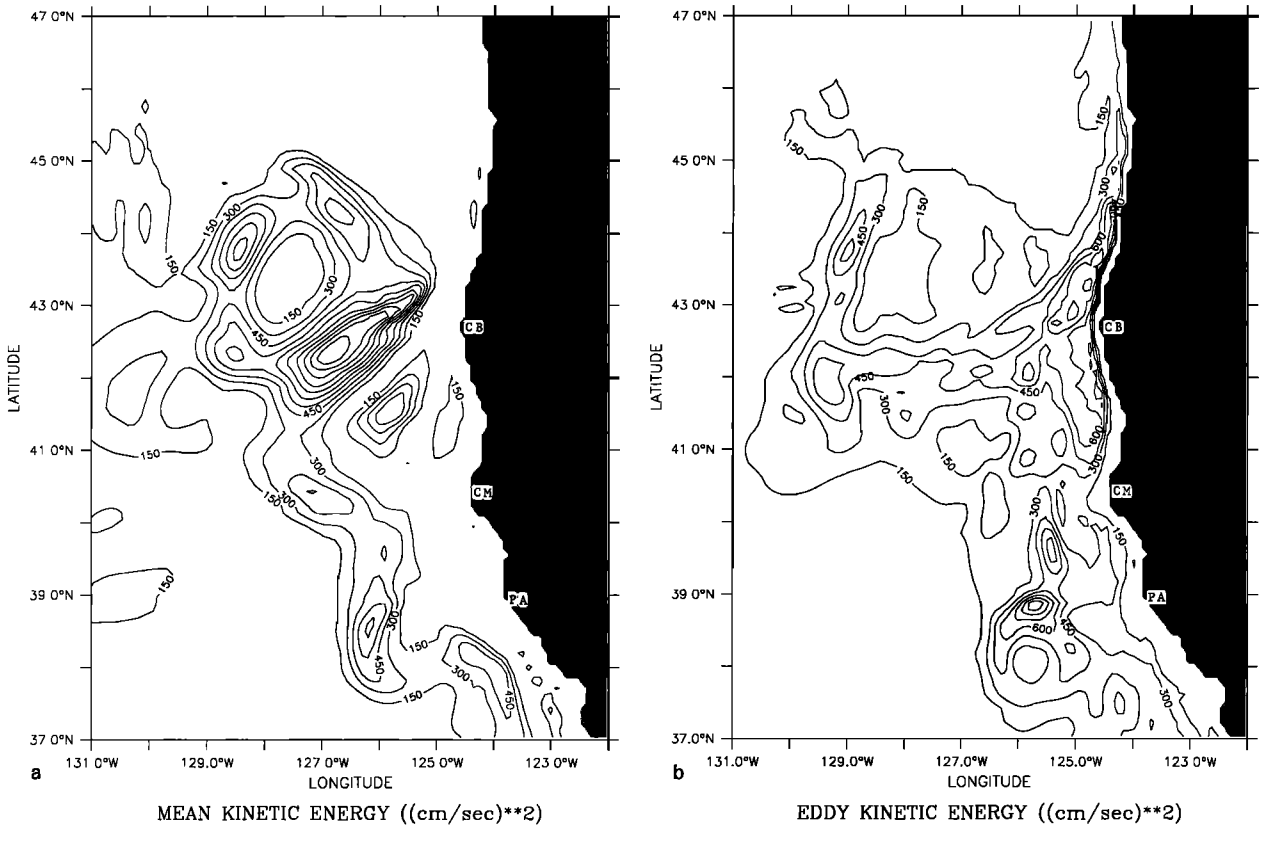

Figure 16. (a) Mean and (b) eddy kinetic energy for experiment 3 at 46 m depth. Contour interval is 150 cm^2/s^2.

of the meandering jet from the coastal waters off Oregon. With the return of upwelling favorable winds in the spring, the coastal equatorward current develops along the Oregon coast, flows offshore in the vicinity of Cape Blanco, and redevelops a meandering jet downstream. South of Cape Blanco and inshore of the meandering jet, both anticyclonic and cyclonic eddies develop throughout the upwelling season (e.g., Figures 14a and 14b). As they propagate westward, they become embedded in the meandering jet, leading to strong onshore and offshore transports in the coastal region.

On the basis of these results, it is seen that the phenomenonological behavior of the model simulations is qualitatively similar to large-scale observational data in the CCS. This lends support to our hypothesis that both wind forcing and coastline irregularities are key mechanisms for the generation, evolution, and maintenance of the currents, as well as for the intense and complex meander, eddy, jet, and filament structures in the CCS.

Acknowledgments. This work was done in the Department of Oceanography at the Naval Postgraduate School under the support of the National Science Foundation, through contract OCE-9203325. Aid with the plots by Peter Braccio, Mike Cook, and Ming-Jer Huang is greatly appreciated. We also thank Tim Stanton and Tom Herbers for letting us run the model on their Hewlett-Packard workstations. We wish to thank Jeff Paduan, Curt Collins, Tim Stanton, and the reviewers for valuable comments.

References

Adamec, D., The treatment of mixing processes in advective models, in *Advanced Physical Oceanographic Numerical Modeling*, edited by J. J. O'Brien, pp. 495–510, D. Reidel, Norwell, Mass., 1986.

Adamec, D., R. L. Elsberry, R. W. Garwood Jr. and R. L. Haney, An embedded mixed layer-ocean circulation model, *Dyn. Atmos. Oceans*, *5*, 69–96, 1981.

Allen, J. S., L. J. Walstad, and P. A. Newberger, Dynamics of the coastal transition zone jet, 2, Nonlinear finite-amplitude behavior, *J. Geophys. Res.*, *96*, 14,995–15,016, 1991.

Arakawa, A., and V. R. Lamb, Computational design of the basic dynamical processes of the UCLA general circulation model, *Methods Comput. Phys.*, *17*, 173–265, 1977.

Arthur, R. S., On the calculation of vertical motion in eastern boundary currents from determinations of horizontal motion, *J. Geophys. Res.*, *70*, 2799–2803, 1965.

Auad, G., A. Pares-Sierra, and G. K. Vallis, Circulation and energetics of a model of the California Current system, *J. Phys. Oceanogr.*, *21*, 1334–1552, 1991.

Batteen, M. L., Model simulations of a coastal jet and undercurrent in the presence of eddies and jets in the California Current system, in *Poleward Flows Along Eastern Ocean Boundaries*, edited by S. J. Neshyba, C. N. K. Mooers, R. L. Smith, and R. T. Barber, pp. 263–279, Springer-Verlag, New York, 1989.

Batteen, M. L., and Y.-J. Han, On the computational noise of finite-difference schemes used in ocean models, *Tellus*, *33*, 387–396, 1981.

Batteen, M. L., and M. J. Rutherford, Modeling studies of eddies in the Leeuwin Current: The role of thermal forcing, *J. Phys. Oceanogr.*, *20*, 1484–1520, 1990.

Batteen, M. L., R. L. Haney, T. A. Tielking, and P. G. Renaud, A numerical study of wind forcing of eddies and jets in the California Current system, *J. Mar. Res.*, *47*, 493–523, 1989.

Batteen, M. L., M. J. Rutherford, and E. J. Bayler, A numerical study of wind and thermal forcing effects on the ocean circulation off Western Australia, *J. Phys. Oceanogr.*, *22*, 1406–1433, 1992a.

Batteen, M. L., C. N. Lopes da Costa, and C. S. Nelson, A numerical study of wind stress curl effects on eddies and filaments off the northwest coast of the Iberian Peninsula, *J. Mar. Syst.*, *3*, 249–266, 1992b.

Batteen, M. L., C.-P. Hu, J. L. Bacon, and C. S. Nelson, A numerical study of wind forcing on the Chile Current system, *J. Oceanogr.*, *51*, 585–614, 1995.

Bernstein, R. L., L. C. Breaker, and R. Whritner, California Current eddy formation: Ship, air, and satellite results, *Science*, *195*, 353–359, 1977.

Blumberg, A. F., and G. L. Mellor, A description of a three-dimensional coastal ocean circulation model, in *Three-Dimensional Ocean Models*, *4*, Coastal Estuarine Stud., vol. 4, edited by N. Heaps, pp. 1–16, AGU, Washington, D. C., 1987.

Breaker, L. C., and C. N. K. Mooers, Oceanic variability off the central California coast, *Prog. Oceanogr.*, *17*, 61–135, 1986.

Brink, K. H., and T. J. Cowles, The Coastal Transition Zone program, *J. Geophys. Res.*, *96*, 14,637–14,647, 1991.

Camerlengo, A. L., and J. J. O'Brien, Open boundary conditions in rotating fluids, *J. Comput. Phys.*, *35*, 12–35, 1980.

Chelton, D. B., Seasonal variability of alongshore geostrophic velocity off central California, *J. Geophys. Res.*, *89*, 3473–3486, 1984.

Flament, P., L. Armi, and L. Washburn, The evolving structure of an upwelling front, *J. Geophys. Res.*, *90*, 11,765–11,778, 1985.

Freitag, H. P., and D. Halpern, Hydrographic observations off northern California during May 1977, *J. Geophys. Res.*, *86*, 4248–4252, 1981.

Haidvogel, D. B., A. Beckmann, and K. S. Hedstrom, Dynamical simulation of filament formation and evolution in the coastal transition zone, *J. Geophys. Res.*, *96*, 15,017–15,040, 1991.

Han, Y.-J., Numerical simulation of mesoscale eddies, Ph.D. thesis, 154 pp., Univ. of Calif., Los Angeles, 1975.

Haney, R. L., A numerical study of the response of an idealized ocean to large-scale surface heat and momentum flux, *J. Phys. Oceanogr.*, *4*, 145–167, 1974.

Hickey, B. M., The California Current system—Hypothesis and facts, *Prog. Oceanogr.*, *8*, 191–279, 1979.

Hickey, B. M., Western North America, Tip of Baja California to Vancouver Island, in *The Sea*, John Wiley, New York, in press, 1996.

Holland, W. R., The role of mesoscale eddies in the general circulation of the ocean—Numerical experiments using a wind-driven quasi-geostrophic model, *J. Phys. Oceanogr.*, *8*, 363–392, 1978.

Holland, W. R., and M. L. Batteen, The parameterization of subgrid scale heat diffusion in eddy-resolved ocean circulation models, *J. Phys. Oceanogr.*, *16*, 200–206, 1986.

Holland, W. R., and L. B. Lin, On the generation of mesoscale eddies and their contribution to the general circulation, II, A parameter study, *J. Phys. Oceanogr.*, *5*, 658–699, 1975.

Holland, W. R., D. E. Harrison, and A. J. Semtner Jr., Eddy-resolving numerical models of large-scale ocean circulation, in *Eddies in Marine Science*, edited by A. R. Robinson, pp. 379–403, Springer-Verlag, New York, 1983.

Huyer, A., P. M. Kosro, J. Fleischbein, S. R. Ramp, T. Stanton, L. Washburn, F. P. Chavez, T. J. Cowles, S. D. Pierce, and R. L. Smith, Currents and water masses of the coastal transition zone off northern California, June to August 1988, *J. Geophys. Res.*, *96*, 14,809–14,831, 1991.

Ikeda, M., and W. J. Emery, Satellite observations and modeling of meanders in the California Current system off Oregon and northern California, *J. Phys. Oceanogr.*, *14*, 1434–1450, 1984.

Ikeda, M., W. J. Emery, and L. A. Mysak, Seasonal variability in meanders of the California Current system off Vancouver Island, *J. Geophys. Res.*, *89*, 3487–3505, 1984a.

Ikeda, M., L. A. Mysak, and W. J. Emery, Observations and modeling of satellite-sensed meanders and eddies off Vancouver Island, *J. Phys. Oceanogr.*, *14*, 3–21, 1984b.

Kelly, K. A., The influence of winds and topography on the sea surface temperature patterns over the northern California slope, *J. Geophys. Res.*, *90*, 11,783–11,798, 1985.

Kosro, P. M., and A. Huyer, CTD and velocity surveys of seaward jets off northern California, July 1981 and 1982, *J. Geophys. Res.*, *91*, 7680–8690, 1986.

McCreary, J. P., and P. K. Kundu, Western boundary circulation during an alongshore wind: With application to the Somali Current system, *J. Mar. Res.*, *43*, 493–516, 1985.

McCreary, J. P., Y. Fukamachi, and P. K. Kundu, A numerical investigation of jets and eddies near an eastern ocean boundary, *J. Geophys. Res.*, *96*, 2515–2534, 1991.

Mooers, C. N. K., and A. R. Robinson, Turbulent jets and eddies in the California Current and inferred cross-shore transports, *Science*, *223*, 51–53, 1984.

Narimousa, S., and T. Maxworthy, Two-layer model of shear-driven

coastal upwelling in the presence of bottom topography, *J. Fluid Mech.*, *159*, 503–531, 1985.

Narimousa, S., and T. Maxworthy, Application of a laboratory model to the interpretation of satellite and field observations of coastal upwelling, *Dyn. Atmos. Oceans*, *13*, 1–46, 1989.

Pares-Sierra, A., W. B. White, and C.-K. Tai, Wind-driven coastal generation of annual mesoscale eddy activity in the California Current system: A numerical model, *J. Phys. Oceanogr.*, *23*, 1110–1121, 1993.

Paulson, C. A., and J. J. Simpson, Irradiance measurements in the upper ocean, *J. Phys. Oceanogr.*, *7*, 952–956, 1977.

Pierce, S. D., J. S. Allen, and L. J. Walstad, Dynamics of the coastal upwelling zone jet, 1, Linear stability analysis, *J. Geophys. Res.*, *96*, 14,979–14,993, 1991.

Reid, J. L., Physical oceanography, 1947–1987, *CalCOFI Rep. 29*, pp. 42–65, Calif. Coop. Oceanic Fish. Invest., La Jolla, 1988.

Rienecker, M. M., and C. N. K. Mooers, A summary of the OPTOMA program's mesoscale ocean prediction studies in the California Current system, in, *Mesoscale/Synoptic Coherent Structures in Geophysical Turbulence*, edited by J. C. J. Nihoul and B. M. Jamart, pp. 519–548, Elsevier Sci., New York, 1989.

Rienecker, M. M., C. N. K. Mooers, D. E. Hagan, and A. R. Robinson, A cool anomaly off northern California: An investigation using IR satellite imagery and in situ data, *J. Geophys. Res.*, *90*, 4807–4818, 1985.

Rienecker, M. M., C. H. Reed, and C. N. K. Mooers, Mesoscale variability in the California Current system during 1982 to 1986: Maps of surface dynamic height, sea surface temperature at 50 m depth, mixed layer depth and depth of the 8C isotherm from observations during the OPTOMA program, *INO Tech. Rep. 87-01*, 138 pp., Inst. for Nav. Oceanogr., Stennis Space Center, Miss., 1988.

Robinson, A. R., J. A. Carton, C. N. K. Mooers, L. T. Walstad, E. F. Carter, M. M. Rienecker, J. A. Smith, and W. G. Leslie, A real-time dynamical forecast of ocean synoptic/mesoscale eddies, *Nature*, *309*, 781–783, 1984.

Semtner, A. J., Jr., and Y. Mintz, Numerical simulation of the Gulf Stream and midocean eddies, *J. Phys. Oceanogr.*, *7*, 208–230, 1977.

Strub, P. T., and C. James, The large-scale summer circulation of the California Current, *Geophys. Res. Lett.*, *22*, 207–210, 1995.

Strub, P. T., P. M. Kosro, A. Huyer, and CTZ Collaborators, The nature of the cold filaments in the California Current system, *J. Geophys. Res.*, *96*, 14,743–14,768, 1991.

Trenberth, K. E., W. G. Large, and J. G. Olson, The mean annual cycle in global ocean wind stress, *J. Phys. Oceanogr.*, *20*, 1742–1760, 1990.

Walstad, L. J., J. S. Allen, P. M. Kosro, and A. Huyer, Dynamics of the coastal transition zone through data assimilation studies, *J. Geophys. Res.*, *96*, 14,959–14,977, 1991.

Weatherly, G. L., A study of the bottom boundary layer of the Florida Current, *J. Phys. Oceanogr.*, *2*, 54–72, 1972.

M. L. Batteen, Department of Oceanography, Naval Postgraduate School, Monterey, CA 93943-5000. (e-mail: batteen@oc.nps.navy.mil)

(Received October 13, 1995; revised July 30, 1996;
accepted September 9, 1996.)